A Multi-Wavelength Study of Low Redshift Clusters of Galaxies II. Environmental Impact on Galaxy Growth

David W. Atlee[1] and Paul Martini

Department of Astronomy, The Ohio State University
4055 McPherson Laboratory, 140 W. 18th Ave., Columbus, OH 43210, USA

atlee@astronomy.ohio-state.edu

ABSTRACT

Galaxy clusters provide powerful laboratories for the study of galaxy evolution, particularly the origin of correlations of morphology and star formation rate (SFR) with density. We construct visible to MIR spectral energy distributions (SEDs) of cluster galaxies and use them to measure stellar masses and SFRs in eight low redshift clusters, which we examine as a function of environment. A partial correlation analysis indicates that SFR depends strongly on R/R_{200} ($> 99.9\%$ confidence) and is independent of projected local density at fixed radius. SFR also shows no residual dependence on stellar mass. We therefore conclude that interactions with the intra-cluster medium drive the evolution of SFRs in cluster galaxies. A merged sample of galaxies from the five most complete clusters shows $\langle SFR \rangle \propto (R/R_{200})^{1.3\pm0.7}$ for galaxies with $R/R_{200} \leq 0.4$. A decline in the fraction of SFGs toward the cluster center contributes most of this effect, but it is accompanied by a reduction in SFRs among star-forming galaxies (SFGs) near the cluster center. The increase in the fraction of SFGs toward larger R/R_{200} and the isolation of SFGs with reduced SFRs near the cluster center are consistent with ram pressure stripping as the mechanism to truncate star formation in galaxy clusters. We conclude that stripping drives the properties of SFGs over the range of radii we examine. We also find that galaxies near the cluster center are more massive than galaxies farther out in the cluster at $\sim 3.5\sigma$, which suggests that cluster galaxies experience dynamical relaxation during the course of their evolution.

Subject headings: galaxies:clusters:general, galaxies:evolution, galaxies:star formation, infrared radiation

---

[1]The National Optical Astronomy Observatory, 950 N. Cherry Avenue, Tucson AZ 85719

1. Introduction

The current paradigm for the evolution of the universe and the growth of structure is based largely on observations of the luminous matter in the universe, i.e. individual galaxies, groups and clusters, and the cosmic microwave background. While galaxy formation physics could previously be neglected, the era of precision cosmology increasingly demands detailed knowledge of galaxy formation to map observations of luminous matter onto dark matter halos (e.g. van Daalen et al. 2011). To do so precisely, we must understand the relationship between galaxy evolution and environment.

Galaxy formation theory dates to the middle of the twentieth century. Early work explored the physical processes responsible for star-formation (Whipple 1946), speculated about the origins of the Milky Way (Eggen et al. 1962), and examined the impact of environment on galaxy evolution (Spitzer & Baade 1951). Osterbrock (1960) discovered that star-forming galaxies (SFGs) are less common in galaxy clusters than in lower density environments, and this result was subsequently re-examined with larger samples (Gisler 1978; Dressler et al. 1985). The dearth of vigorous star formation in galaxy clusters is mirrored by an under-abundance of spiral galaxies in these high density regions, known as the morphology-density relation (Dressler 1980; Postman & Geller 1984; Dressler et al. 1997; Postman et al. 2005).

The impact of environment on the frequency and intensity of star-formation has been studied intensely in galaxy clusters and also at a variety of other density scales. These measurements have employed both visible wavelength colors (Kodama & Bower 2001; Balogh et al. 2004; Barkhouse et al. 2009; Hansen et al. 2009) and emission lines (Abraham et al. 1996; Balogh et al. 1997, 2000; Kauffmann et al. 2004; Christlein & Zabludoff 2005; Poggianti et al. 2006; Verdugo et al. 2008; Braglia et al. 2009; von der Linden et al. 2010) as well as mid-infrared (MIR) luminosities (Bai et al. 2006; Saintonge et al. 2008; Bai et al. 2009). SFGs are consistently found to be more common and to have higher SFRs in lower density environments and at higher redshifts (Kauffmann et al. 2004; Poggianti et al. 2006, 2008). This trend appears to reverse by $z \approx 2$, with star formation more common in clusters than in the field (Tran et al. 2010; Hatch et al. 2011). However, even high-z cluster galaxies form their stars earlier than coeval field galaxies (Rettura et al. 2011), which is an expression of the so-called "downsizing" phenomenon (Cowie et al. 1996).

The relationships between SFR, morphology and environment in the local universe place strong constraints on models for galaxy evolution. Another important factor is the presence of an evolutionary trend for galaxies to have higher SFRs at higher redshifts. This was originally reported as an excess of blue cluster members at $z \approx 0.4$ compared to $z = 0$ (Oemler 1974; Butcher & Oemler 1978, 1984), and is commonly known at the Butcher-

Oemler Effect. This trend is now understood to track the simultaneous increase in the fraction of star-forming galaxies (SFGs) and in the SFRs of individual SFGs. An analogous trend has been examined in the MIR (Saintonge et al. 2008; Haines et al. 2009; Tran et al. 2010; Hatch et al. 2011), which is sensitive to dust-enshrouded star formation.

The observed trends in star formation with environment and the variation of these trends with redshift are usually attributed to changes in the sizes of cold gas reservoirs. Several mechanisms have been proposed to reduce galaxies' cold gas supplies and transform them from SFGs to passive galaxies. These mechanisms include ram-pressure stripping of cold gas (RPS; Gunn & Gott 1972; Abadi et al. 1999; Quilis et al. 2000; Roediger & Hensler 2005; Roediger & Brüggen 2006, 2007; Jáchym et al. 2007), gas starvation (Larson et al. 1980; Balogh et al. 2000; Bekki et al. 2002; Kawata & Mulchaey 2008; McCarthy et al. 2008; Book & Benson 2010), galaxy harassment (Moore et al. 1996, 1998; Lake et al. 1998), and interactions with the cluster tidal potential (Merritt 1983, 1984; Natarajan et al. 1998). Gas starvation operates throughout clusters, and it converts galaxies from star forming to passive on a gas exhaustion timescale, which, for normal spiral galaxies, is ~ 2.5 Gyr (Bigiel et al. 2011). This time is similar to the cluster crossing time of 2.4 Gyr, which is the timescale appropriate for dynamical processes like galaxy harassment. These timescales contrast sharply with the timescale appropriate for RPS, which truncates star formation on a gas stripping timescale, which is of order 10^5 yr. The efficiency of RPS also scales with ICM density, so it operates much more strongly near cluster centers than either starvation or harassment. These differences mean that how rapidly star formation declines in cluster galaxies relative to the field constrains the mechanism primarily responsible for the removal of cold gas from cluster galaxies.

The variation of SFR with environment can probe the relative importance of different environmental processes, but the conclusions drawn from apparently similar observations sometimes conflict. For example, Moran et al. (2007) identified passive spirals in a sample of $z \approx 0.5$ clusters and determined that spiral galaxies rapidly turn passive when they enter the cluster environment and then evolve into S0 galaxies. Bai et al. (2009) argue that the similarity of the $24\mu m$ luminosity functions observed in galaxy clusters and in the field suggests that the transition from star-formation to quiescence must be rapid, which implies that ram pressure stripping (RPS) is the dominant mechanism. Verdugo et al. (2008) and von der Linden et al. (2010), by contrast, find a significant trend of increasing SFR with radius to at least $2R_{200}$ from cluster centers. Because the trend of SFR with radius appears to extend to the virial shock (White & Frenk 1991), von der Linden et al. (2010) conclude that preprocessing at the group scale is important. Patel et al. (2009) find a similar trend for increasing average SFR with decreasing local density down to group-scale densities ($\Sigma_{gal} \approx 1.0$ Mpc^{-2}).

Evidence for pre-processing in groups is important because RPS is inefficient in low density gas, so preprocessing (Zabludoff & Mulchaey 1998; Fujita 2004) is likely driven by processes like gas starvation that operate in less dense environments. While preprocessing appears to be important in some groups and clusters, Berrier et al. (2009) found that very few cluster galaxies have previously resided in groups, so the impact of preprocessing on a typical cluster galaxy must be limited.

In Atlee et al. (2011; henceforth Paper I), we developed a multi-wavelength method to identify AGNs based on either their X-ray luminosities or the shapes of their visible-MIR spectral energy distributions (SEDs). In this paper, we will employ this method to correct for AGNs and measure star formation in cluster galaxies. We use the results to study the relationship between star formation and the cluster environment. In particular, we consider the constraints placed on the important environmental processes that operate in clusters by the distribution of star formation among cluster members.

The paper is organized as follows: In §2, we review our observations, which are discussed in more detail in Paper I. In §3 we review the mathematical formalism associated with partial correlation analysis. In §4 we derive completeness corrections for the observed cluster members. We discuss the derivation of total infrared (TIR) luminosity functions (LFs) in §5, and in §6 we detail the results of our measurements. Finally, we examine the implications of these results for the environmental dependence of galaxy evolution in §7, and we summarize these conclusions in §8. Throughout this paper we adopt the WMAP 5-year cosmology—a Λ-CDM universe with $\Omega_m = 0.26$, $\Omega_\Lambda = 0.74$ and $h = 0.72$ (Dunkley et al. 2009).

2. Observations and Member Description

Paper I provides details of our photometry and spectroscopy. It also develops methods to reliably identify low-luminosity AGNs and to measure galaxy properties like stellar mass and SFRs for identified cluster members, including AGN hosts. We briefly summarize the salient points below.

2.1. Observations

We identified cluster member galaxies using redshifts determined by Martini et al. (2007). We supplemented these with redshifts from the literature, which we obtained from

the NASA Extragalactic Database (NED)[1]. (These redshifts come from a variety of sources with unknown selection functions and success rates. See §4.)

We have visible-wavelength images from the du Pont telescope at Las Campanas observatory, MIR images from the IRAC and MIPS instruments on the *Spitzer Space Telescope*, and X-ray images extracted from the *Chandra* archive. We measure visible, MIR and X-ray fluxes in redshift-dependent photometric apertures that approximate a fixed metric size. The aperture fluxes are then corrected to total fluxes at constant color with the R-band Kron-like magnitude from SExtractor (Bertin & Arnouts 1996). Our photometry spans the peak of the stellar continuum, so we have robust photometric redshifts, which can identify catastrophic errors among the spectroscopic redshifts. We found 12 such catastrophic errors, one of which is an AGN (Paper I). We exclude these objects from our analysis.

2.2. Cluster Member Description and AGN Identification

In Paper I, we constructed spectral energy distributions (SEDs) from the photometry described in §2.1, and we fit models to these fluxes with SED template codes from Assef et al. (2010). These model SEDs are used to derive photometric redshifts and K-corrections. We also employed the models to measure MIR color corrections, and we used the results to determine rest-frame luminosities.

We employ rest-frame, visible wavelength colors to determine the mass to light ratio of each galaxy in the sample (Bell & de Jong 2001), and we combine these with the measured luminosities to infer M_*. To measure SFRs, we employ both $8\mu m$ and $24\mu m$ luminosities (Zhu et al. 2008). When SFRs can be measured in both bands, we take the geometric mean of the two measurements. We found in Paper I that SFRs determined independently from $8\mu m$ and $24\mu m$ luminosities show a scatter of ~ 0.2 dex with respect to one another. This scatter reflects the systematic uncertainty in SFR measurements determined from either band separately, and the implied uncertainty is comparable to the systematic uncertainties in the measured stellar masses (0.3 dex, Paper I).

Before we measure stellar masses and SFRs of cluster members, we identify and correct for AGNs. We employ two independenty methods to identify AGNs: the shapes of the model SEDs (IR AGNs) and the X-ray luminosities measured with *Chandra* (X-ray AGNs). The hosts of IR AGNs are corrected for the presence of the AGN before we calculate M_* and SFR. X-ray AGNs without visible signatures in their SEDs do not contribute significantly

[1]http://nedwww.ipac.caltech.edu/

to the measured visible and MIR fluxes, so we do not correct those objects. In Paper I, we found that the IR and X-ray AGN samples are largely disjoint. This implies that X-ray only AGN selection can overlook a large fraction ($\sim 35\%$) of AGNs. We explore the potential consequences of this bias in §6.5 and §6.6.

3. Partial Correlation Analysis

When confronted with a system of mutually correlated observables, it can be difficult to establish which variables drive the correlations. Partial correlation analysis measures the relationship between two variables with all other parameters held fixed and can identify which variable(s) control the observed correlations. Partial correlation analysis has been applied in the past to develop a fundamental plane of black hole activity (Merloni et al. 2003) and to probe the dependence of SFR on both stellar mass and environment simultaneously (Christlein & Zabludoff 2005). We will use the simplest formulation of partial correlation analysis, which relies only on direct measurements and does not account for upper limits.

The simplest case is a system of only three variables, x_i. This is called the first-order partial correlation problem. The correlation coefficient for x_1 and x_2 at fixed x_3 can be expressed as

$$r_{12.3} = \frac{\rho_{12} - \rho_{13}\rho_{23}}{\sqrt{(1-\rho_{13}^2)(1-\rho_{23}^2)}} \tag{1}$$

where ρ_{ij} is the standard two-variable correlation coefficient (e.g. the Pearson or Spearman coefficients) between x_i and x_j (Wall & Jenkins 2003). Higher order problems describe systems with more variables. For a system of N variables, the $(N-2)^{th}$ order partial correlation coefficient $r_{ij.1\ldots N\setminus\{ij\}}$ of variables x_i and x_j can be written,

$$r_{ij.1\ldots N\setminus\{ij\}} = \frac{-C_{i,j}}{\sqrt{C_{i,i}C_{j,j}}} \tag{2}$$

where $C_{i,j} = (-1)^{i+j}M_{i,j}$ (Kendell & Stuart 1977). $M_{i,j}$ is a reduced determinant of the correlation matrix R, where $R_{i,j} = \rho_{ij}$, and ρ_{ij} is the two-variable correlation coefficient of x_i and x_j. The determinant $M_{i,j}$ can be interpreted as the total correlation among the variables of the system in the absence of i and j. It is calculated from R with the i^{th} row and j^{th} column eliminated (Kendell & Stuart 1977).

Given a partial correlation coefficient from Eq. 2, we would like to know its significance. This can be evaluated from $\sigma_{ij.1\ldots N\setminus\{ij\}}$,

$$\sigma_{ij.1\ldots N\setminus\{ij\}} = \frac{1 - r_{ij.1\ldots N\setminus\{ij\}}}{\sqrt{m-N}} \tag{3}$$

where $r_{ij.1...N\backslash\{ij\}}$ is the partial correlation coefficient given by Eq. 2, N is the number of variables in the system, and m is the number of objects in the sample. The statistical significance of $r_{ij.1...N\backslash\{ij\}}$ is determined from the Student's t-distribution with dispersion $\sigma_{ij.1...N\backslash\{ij\}}$ (Wall & Jenkins 2003).

Partial correlation analyses can take both parametric and non-parametric forms. These are analogous to the more commonly applied two-variable correlation analyses. Equation 2 can be applied to any of the correlation coefficients in common use. However, Eq. 3 is defined for the parametric Pearson's correlation coefficient, so it is appropriate only for that estimator or the closely related, non-parametric Spearman coefficient. We want a non-parametric approach, so we rely on Spearman correlation coefficients in our analysis.

4. Completeness Corrections

We wish to examine the distributions of the stellar masses and SFRs described in §2.2 to probe the impact of the cluster environment on galaxy growth. However, to do this we must first correct for selection effects. The spectroscopic selection function that defines our sample is unknown, because many of the sources that contribute to the redshifts in the literature do not define their target selection functions or rates of success. Furthermore, the MIR observations do not uniformly cover the cluster fields. Therefore, we empirically determine both our spectroscopic and MIR selection functions to correct for these effects.

4.1. Spectroscopic Completeness

We examine only spectroscopically-confirmed cluster members. Many of the redshifts we use come from Martini et al. (2007), which we supplemented with redshifts from other sources in the literature. This results in a complex selection function that is poorly known *a priori*. However, this completeness function is required to correct the properties of observed cluster galaxies to the intrinsic distribution for all cluster members. We take an empirical approach to determine spectroscopic completeness and correct the measured cluster members to the total cluster galaxy population.

For each cluster, we bin galaxies identified in the photometric source catalog by $V - R$ color, R-band magnitude and R/R_{200}. We find significant variations in the fraction of galaxies with spectra (f_{spec}) as a function of R/R_{200} and m_R, but the variation with color is at most minor. A partial correlation analysis of f_{spec} as a function of color, magnitude and position shows no significant partial correlation with $V - R$ at 95% confidence in any cluster, while

f_{spec} correlates with both m_R and R/R_{200} at $> 99.9\%$ confidence. We therefore collapse the measurement along the color axis and determine the fraction of galaxies with spectroscopy as a function of R-magnitude and position only. This results in better measurements due to the larger number of galaxies per bin.

The f_{spec} measured above is one way to express the spectroscopic completeness of galaxies in a given magnitude-radius bin. However, what we really want is an expression for the spectroscopic completeness, C_{spec}, of cluster members,

$$C_{spec}(\vec{x}) = \frac{N_{Cl,spec}(\vec{x})}{N_{Cl}(\vec{x})} \quad (4)$$

$$= \frac{N_{spec}(\vec{x})}{N_{tot}(\vec{x})} \times \frac{N_{Cl,spec}(\vec{x})}{N_{spec}(\vec{x})} \times \frac{N_{tot}(\vec{x})}{N_{Cl}(\vec{x})} \quad (5)$$

where $\vec{x}$ is the position of a given bin in magnitude-radius space, $N_{Cl,spec}$ is the number of galaxies with spectra that are cluster members, N_{Cl} is the number of true cluster members, N_{spec} is the number of galaxies with spectra in the cluster field, and N_{tot} is the number of galaxies in the input catalog. All of these quantities except N_{Cl} can be measured directly from the input catalogs. We would need to infer N_{Cl} using some additional piece of information, so we prefer to rely on f_{spec} rather than C_{spec} if possible.

If the redshifts reported in the literature were not pre-selected for cluster membership or if the redshift failure rate was high, $f_{spec}(\vec{x})$ would be a good proxy for $C_{spec}(\vec{x})$, and the approach in Eq. 4 would be unnecessary. If this were the case, the fraction of galaxies with spectra that are cluster members (f_{mem}) should drop with R/R_{200} as the fraction of field galaxies increases. Figure 1 shows that f_{mem} does not always trace the decline in the density of cluster galaxies. This implies that f_{spec} is not a good tracer of C_{spec}, and the more sophisticated approach of Eq. 4 is required.

Before we can employ Eq. 4, we need to know the number of cluster galaxies in each bin. To do this, we estimate the number of field galaxies in the bin with the R-band magnitude-number density relation reported by Kümmel & Wagner (2001). We subtract the field galaxies from the total number of galaxies in the bin to estimate the number of cluster galaxies.

This approach introduces two types of uncertainty. The first is simple Poisson counting uncertainty due to the small number of field galaxies, typically a few to 10, in each bin. The second is cosmic variance. Ellis (1987) reports a B-band magnitude-number relation that includes measurements from a number of other authors. The different surveys use fields of different sizes, so the scatter of their results about the best-fit relation provide a measure of the cosmic variance, which contributes of order 10% uncertainty on the number of field

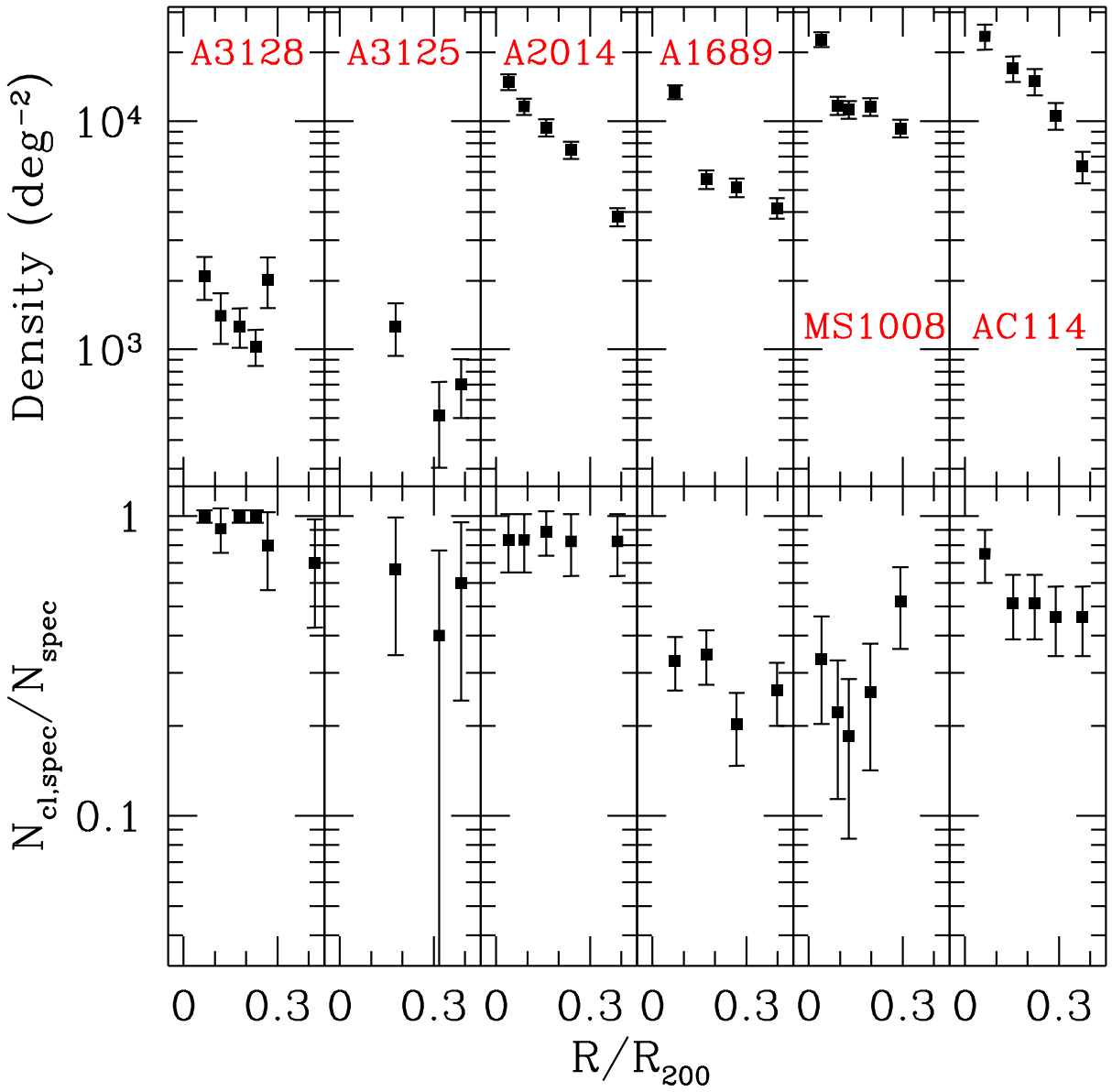

Fig. 1.—: Comparison of galaxy density (*upper panel*) and spectroscopic membership fraction (*lower panel*) as a function of radius for the clusters in our sample with enough confirmed members to make a meaningful measurement. If f_{spec} were a good proxy for $f_{Cl,spec}$, the upper and lower panels would have similar slopes. None of the clusters in the sample exhibit this behavior.

galaxies in a typical bin. The number of field galaxies in a given bin depends on magnitude and cluster mass, but it generally ranges from 1-10 galaxies. At faint magnitudes, the number of field galaxies is generally comparable to the number of cluster galaxies, and Poisson fluctuations in the number of field galaxies dominate the uncertainties in the completeness measurements. The spectroscopic completeness measurements and associated uncertainties for each cluster are summarized in Table 1.

Figure 2 shows the spectroscopic completeness (C_{spec}) for 6 of the 8 galaxy clusters in our sample. The remaining 2 clusters (A644 and A2163) have too few confirmed members to make a reliable measurement. The dashed, vertical lines on the right column of Figure 2 indicate the observed magnitude that corresponds to $M_R = -20$ for the average K-correction in each cluster. The follow-up spectroscopy of X-ray sources conducted by Martini et al. (2006) is only complete to this luminosity limit. Clearly, completeness becomes quite poor for $M_R > -20$ in all clusters, so we restrict our sample to galaxies with $M_R < -20$.

We also considered completeness as a function of luminosity and stellar mass instead of m_R. However, these quantities have higher uncertainties than observed magnitudes, especially for galaxies without spectroscopic redshifts to fix their distances. Therefore, we measure completness as a function of m_R and R/R_{200}.

4.2. Mid-Infrared Completeness

The depth of the MIR images varies as a function of position across the clusters. This is a result of the *Spitzer* mosaicking schemes, which were chosen to provide good coverage of the known X-ray point sources in the cluster. These mosaic schemes lead to variations in the number of overlapping images, and therefore to variations in sensitivity, across the cluster fields.

In addition to these sensitivity variations, the *Spitzer* footprint features some non-overlapping coverage by the different IRAC bands. This results from the IRAC mapping strategy, which simultaneously images two adjacent fields in different bands. The pointings chosen by the observer then determine the degree of overlap between the IRAC channels. For a galaxy to enter the final sample, it must include detections in at least 5 bands to ensure that the fit results for that galaxy are well constrained. This means that a faint galaxy in a region of a cluster with overlapping $3.6\mu m$ and $4.5\mu m$ images, for example, might be more likely to appear in the final sample than an identical galaxy in a part of the cluster with only $4.5\mu m$ coverage.

To construct ensemble statistics for whole clusters, we require sensitivity corrections

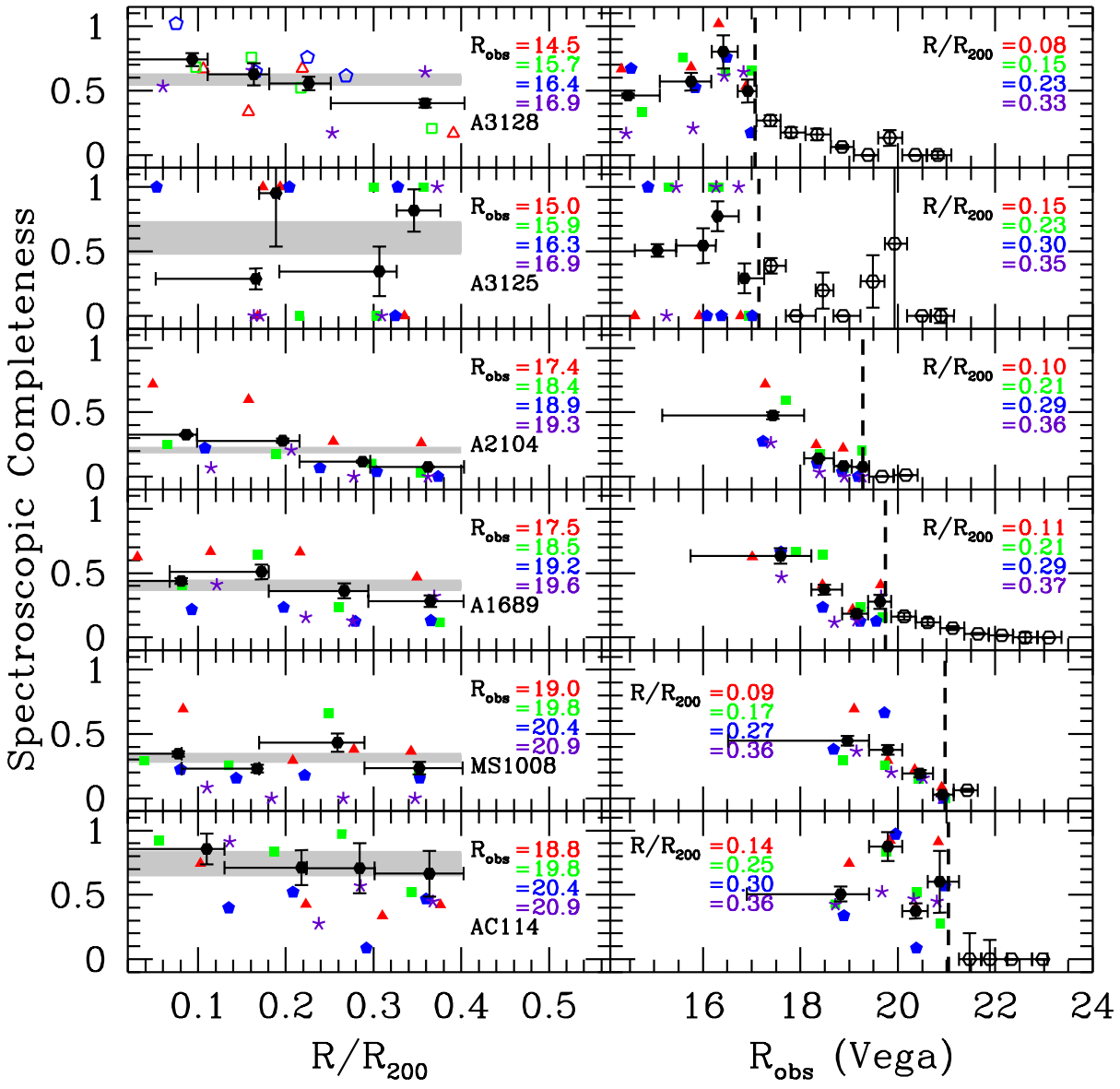

Fig. 2.—: Fraction of cluster galaxies with spectra as a function of projected distance from the cluster center (*left*) and R-band magnitude (*right*). The measurements in each column have been separated by the indicated variable (colored points). The black points show the completeness averaged over all of the colored bins, and the grey bands show the 1σ confidence intervals on the total completeness in each cluster. The dashed, vertical lines on the righthand column indicate the magnitude corresponding to $M_R \approx -20$ mag. The average measurements use only galaxies with $M_R \leq -20$ mag and $R/R_{200} < 0.4$ (*filled, black points*).

that account for variable depth across the cluster fields and for the different footprints in the *Spitzer* bands. We again take an empirical approach to completeness correction. We measure the MIR flux uncertainties at the locations of all confirmed cluster members from the *Spitzer* uncertainty mosaics. At each position, we combine the two Assef et al. (2010) star-forming templates with arbitrary flux normalizations 1000 times to produce galaxies with $10^{-2} < SFR/1\ M_{\odot}\ yr^{-1} < 10^{2}$. From these artificial galaxy SEDs, we construct model fluxes and determine whether the galaxy represented by each SED would have been detected at 3σ based on the flux uncertainty at each position. We bin the results by flux and by R/R_{200} to estimate completeness separately at $8\mu m$ and $24\mu m$. Figure 3 shows the results of this measurement for the 6 clusters in Figure 2. IRAC and MIPS completenesses clearly depend on both flux and R/R_{200}.

The uncertainties in MIR completeness result from the incomplete spectroscopic sampling of the galaxies in a given bin. We implicitly assume that the identified cluster members in each bin are representative of the behavior of the unidentified members. This assumption means that the precision of the completeness correction in a given bin is fixed by the number of identified cluster members in that bin. The completeness we measure, C_{MIR}, is our best estimate of the "true" MIR completeness C_{MIR}^{true} associated with a hypothetical, spectroscopically complete sample of galaxies. In a bin with N cluster members, the expected number of detections is simply $C_{MIR}^{true}N$. However, the actual number of detections will have some range around $C_{MIR}^{true}N$, which leads to an uncertainty in the inversion of C_{MIR} to a completeness correction. This uncertainty is set by the expected variation in the number of galaxies, which is best described by binomial statistics. This allows calculation of asymmetric error bars on C_{MIR} and accounts naturally for upper and lower limits. Typical uncertainties returned by this procedure are $\sim 20\%$. The full set of MIR completeness measurements and the associated uncertainties are summarized in Table 2.

4.3. Merged Cluster Sample

We have defined the MIR completeness measurements in Figure 3 so they apply only to galaxies with spectroscopic redshifts. The two corrections, applied serially, give total completeness corrections. The total correction X_G for a galaxy G is,

$$X_G = \frac{1}{C_{spec}(R_G/R_{200}, m_{R,G})} \times \frac{1}{C_{MIR}(R_G/R_{200}, f_{\nu,G})} \tag{6}$$

where C_{spec} is the spectroscopic completeness (Figure 2) and C_{MIR} is the MIR completeness (Figure 3). The completeness corrections described by Eq. 6 can be applied to individual galaxies to extrapolate from the measured galaxy samples to the full cluster population.

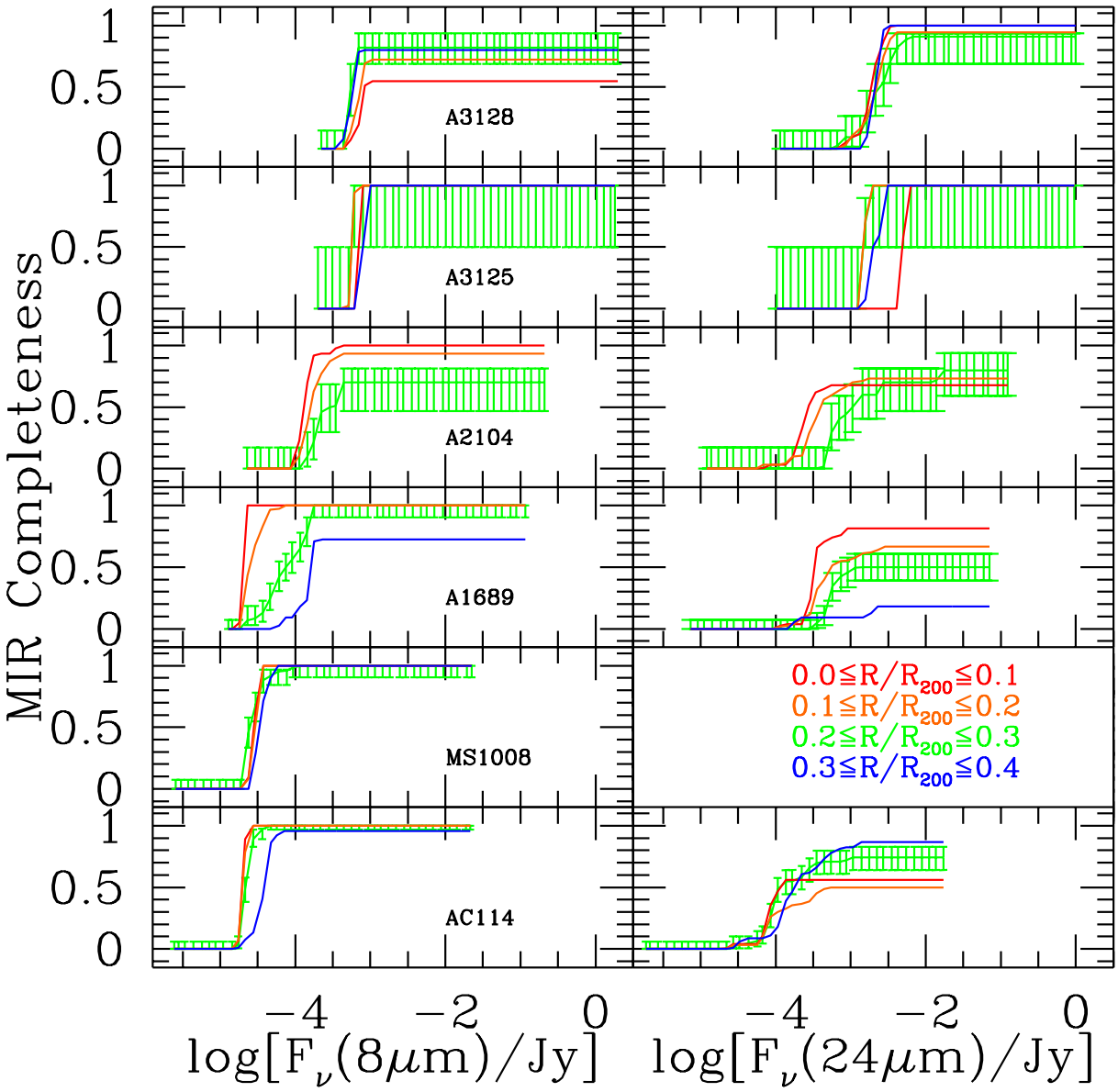

Fig. 3.—: MIR completeness as a function of flux for the 8μm (*left*) and the 24μm (*right*) *Spitzer* bands. In each column, the sample has been separated into 4 radial bins. Fluxes have not been color-corrected and are given in the observer frame. Uncertainties are shown for a single radial bin to indicate typical values. MS 1008.1-1224 was not observed with MIPS. Completeness measurements are derived as described in §4.2.

In cases where multiple corrections can be derived for a single object, we combine these corrections in the same way the data are combined. For example, the completeness correction for a galaxy with SFR measurements from both $8\mu m$ and $24\mu m$ fluxes is given by $X = \left[X_{8\mu m} X_{24\mu m}\right]^{1/2}$ because $SFR = \left[SFR_{8\mu m} SFR_{24\mu m}\right]^{1/2}$ (§2.2).

To examine the dependence of star formation and black hole growth on environment, we need to construct a merged cluster galaxy sample. We identify 5 clusters (A3128, A2104, A1689, MS1008 and AC114) with the best completeness estimates and combine their members. The relatively small number of galaxies in A3125 results in highly irregular behavior of the completeness functions. As a result, any corrections we applied would depend critically on the binning scheme. We therefore exclude it from the main cluster sample.

The clusters in the main sample can be stacked to yield better statistics. To construct the stacked cluster, we weight individual galaxies by their completeness corrections (X_G). The correction is a combination of the spectroscopic and photometric completeness corrections from §4.1 and §4.2, as given by Eqs. 4-6.

5. Luminosity Functions

Luminosity functions (LFs) provide an important diagnostic for the difference between cluster galaxies and field populations, because LFs are sensitive to the entire cluster population rather than only the average. For example, Bai et al. (2009) employed the total infrared (TIR) LF to infer that RPS controls the evolution of SFRs in cluster galaxies. In this section, we discuss the derivation of total infrared (TIR) luminosities and our method to construct luminosity functions. We discuss the results in §6.4.

5.1. Total Infrared Luminosity

Our MIR observations cover a relatively narrow wavelength range from $3.6\mu m$ to $24\mu m$. To compare our results with previous studies, we need to infer L_{TIR} from the observed $L_{8\mu m}$ and $L_{24\mu m}$, so we must apply bolometric corrections (BCs). To estimate L_{TIR} from the *Spitzer* luminosities, we employ the Dale & Helou (2002) SED template library, which includes a wide variety of SEDs. These SEDs differ from one another according to the parameter α, which describes the intensity of the radiation field on a typical dust grain.

Before we calculate BCs for IR AGNs, we first subtract the AGN contribution (Paper I). We then fit each Dale & Helou (2002) template to the rest-frame 5.8, 8.0 and $24\mu m$ fluxes and use the template that best fits the data to measure our fiducial BCs. In the

frequent cases where luminosities in one or more of these bands are unavailable, we estimate the missing luminosities from model SEDs (Assef et al. 2010). When this is necessary, we assign uncertainties to the model fluxes from the uncertainties on the model SED. We only calculate L_{TIR} for galaxies with detections in at least one of the $8\mu m$ and $24\mu m$ bands.

In galaxies that have measurements of both $L_{8\mu m}$ and $L_{24\mu m}$, we calculate L_{TIR} separately for each band and take the geometric mean of the results. This follows our treatment of SFRs in Paper I. In other cases, we simply use the BC appropriate for the band where we have a detection. Typical BCs are ~ 6 for $L_{8\mu m}$ and ~ 8 for $L_{24\mu m}$. We also construct 68% confidence intervals for each BC based on the $\Delta\chi^2 = 1$ interval for each galaxy. These uncertainties are asymmetric, and they add in quadrature to the uncertainties on L_8 and L_{24} to give the total uncertainty on L_{TIR}.

5.2. Luminosity Function Construction

We construct luminosity functions from galaxies in the main cluster sample whose luminosities—$L_{TIR} = L^{+\sigma_u}_{-\sigma_l}$—we determine as described in §5.1. If we account for the uncertainties on L_{TIR}, we can reduce our sensitivity to Poisson fluctuations in the number of luminous galaxies. We distribute the galaxy weights described in §4 over luminosity bins according to the probability that the true luminosity of a galaxy with best-estimate $L = L_{TIR}$ lies in a given bin. Due to the uncertainty on the LF prior, this technique increases the statistical uncertainty on the total weight in each bin by $\sim 10\%$. In exchange, we reduce the much larger uncertainty introduced by stochasticity in the number luminous galaxies.

To distribute galaxy weights over luminosity bins, we employ an asymmetric probability density function (PDF) that considers σ_l and σ_u separately. We integrate the PDF across each luminosity bin to determine the weight in each bin, which we add to construct the total LF. The PDF we employ is piecewise smooth, and it approaches the Normal distribution when $\sigma_u \approx \sigma_l$. It is described in more detail in Appendix A.

In addition to the PDF, we require a prior on the shape of the LF to correct for Eddington-like bias due to the steepness of the LF above L_*. We adopt a Schechter function fit to the Coma cluster LF from Bai et al. (2006) as the baseline prior. We then correct the Coma LF to the redshift of each individual cluster according to the evolution of the field galaxy LF (Le Floc'h et al. 2005). We add the uncertainty on the prior to the statistical uncertainty on the LF in each luminosity bin. The prior has a strong impact on the bright-end shape of the LF because there are few cluster galaxies to constrain the LF in this regime. The results are discussed in §6.4.

6. Results

We apply the weights derived from the completeness corrections described in §4 to the main cluster sample, which is a subset of the cluster galaxies in Table 3. These corrections allow us to examine the average environmental dependence of M_* (§6.2) and SFR (§6.3-6.5), and the redshift dependence of star formation (§6.6). Before conducting these analyses, we perform a partial correlation analysis to determine which observed properties of galaxies in clusters most strongly correlate with star formation (§6.1). The results inform the rest of our work.

6.1. Partial Correlation Analysis

The cluster environment can significantly alter the evolution of cluster member galaxies, as described in §1. However, when we attempt to distinguish between the physical properties that might cause these effects, we confront a system of mutually-correlated observables. For example, SFR depends on both projected local galaxy density to the 10^{th} nearest neighbor (Σ_{10}; Osterbrock 1960; Oemler 1974; Dressler 1980; Kauffmann et al. 2004) and position within the cluster (R/R_{200}; Kodama & Bower 2001; Balogh et al. 2004; Christlein & Zabludoff 2005; Blanton & Berlind 2007; Hansen et al. 2009; von der Linden et al. 2010). Figure 4 demonstrates the correlations between SFR, position, projected galaxy density and M_* among SFGs. It is not immediately clear which of these is the most fundamental.

While the causal connection between morphology and the local density of galaxies is well established (e.g. Dressler 1980; Dressler et al. 1999; Postman et al. 2005), Moran et al. (2007) find strong evidence that the morphologies and star-formation rates of massive spiral galaxies in clusters evolve separately. This implies that a factor other than local density may control star formation in cluster galaxies. Because M_*, R/R_{200} and projected local density (Σ_{10}) are all mutually correlated, it is not easy to determine which variable(s) drive the environmental dependence of star formation. Therefore, we use a partial correlation analysis to disentangle these dependencies. The mathematical formalism for partial correlation analysis is described in §3. We do not consider completeness corrections for this analysis, so we include galaxies from all 8 clusters.

We consider only objects with measurements of all parameters under consideration and ignore galaxies with upper limits. This differs from the similar analysis conducted by Christlein & Zabludoff (2005), who also considered upper limits. As a result, our results are more sensitive than Christlein & Zabludoff (2005) to systematic effects like variations in sensitivity within or between clusters. Because of this, we do not rely directly on the

strength of any partial correlations, but only on the presence or absence of such correlations. For variables with significant partial correlations, we perform stacking analyses, which can account for incompleteness. (See §6.2-§6.6.)

We perform a partial correlation study on a system of five variables: SFR, M_*, R/R_{200}, the Dressler & Shectman (1988) substructure parameter (δ), and projected local density of cluster members (Σ_{10}). The partial correlation coefficients returned by the analysis are listed in Table 4.

Table 4 shows that SFR depends strongly on R/R_{200} ($r_{S,partial} = +0.34$), but it shows no significant dependence of SFR on M_* once the influence of R/R_{200} has been factored out ($r_{S,partial} = +0.09$). This conflicts with earlier results, which generally find either that SFR depends only on M_* (Grützbauch et al. 2011; Rettura et al. 2011) or that SFR depends on both M_* and environment (Christlein & Zabludoff 2005). One reason for this discrepancy is that Table 4 does not include non-SFGs. The fraction of non-SFGs is higher among more massive galaxies, which introduces a dependence of $\langle SFR \rangle$ on M_*. Another possible factor is the difference in stellar masses we examine. The samples of Grützbauch et al. (2011) and Rettura et al. (2011) extend down only to $\sim 3 \times 10^{10} M_\odot$, while our sample extends to approximately $10^{10} M_\odot$. If the cluster environment affects lower mass galaxies more strongly, we should be more sensitive to this effect. Because the efficiency of RPS should depend on M_*, our expanded mass range improves our ability to distinguish between RPS and gas starvation.

Interestingly, SFR also shows no residual dependence on Σ_{10} ($r_{S,partial} = +0.02$), which suggests that the SFRs of cluster members are driven by the local conditions of the ICM rather than by interactions with nearby galaxies. We emphasize that this conclusion applies to SFR only, and we do not consider the dependence of morphology on Σ_{10} or R/R_{200}. This result is also consistent with results from previous authors (Poggianti et al. 1999; Moran et al. 2006, 2007) who found that the processes that alter SFR and morphology are likely to be physically distinct. The determination that SFR is more closely related to R/R_{200} than to Σ_{10} distinguishes our results from those of Christlein & Zabludoff (2005), who do not discriminate between different environmental tracers. As a result, they are agnostic about the process(es) that drive the $\langle SFR \rangle$–radius relation. Our analysis also relies on SFGs alone, which distinguishes it from the work of Christlein & Zabludoff (2005), who included upper limits for galaxies with no measurable star formation. This accounts for the lack of a strong anti-correlation between M_* and SFR, which is driven by a decline in the fraction of SFGs at higher M_* rather than a reduction in the SFRs of individual SFGs.

SFR also shows no relationship to local substructure, as measured by δ, at fixed R/R_{200}. Indeed, even a two-variable correlation test returns no correlation between δ and SFR ($r_S =$

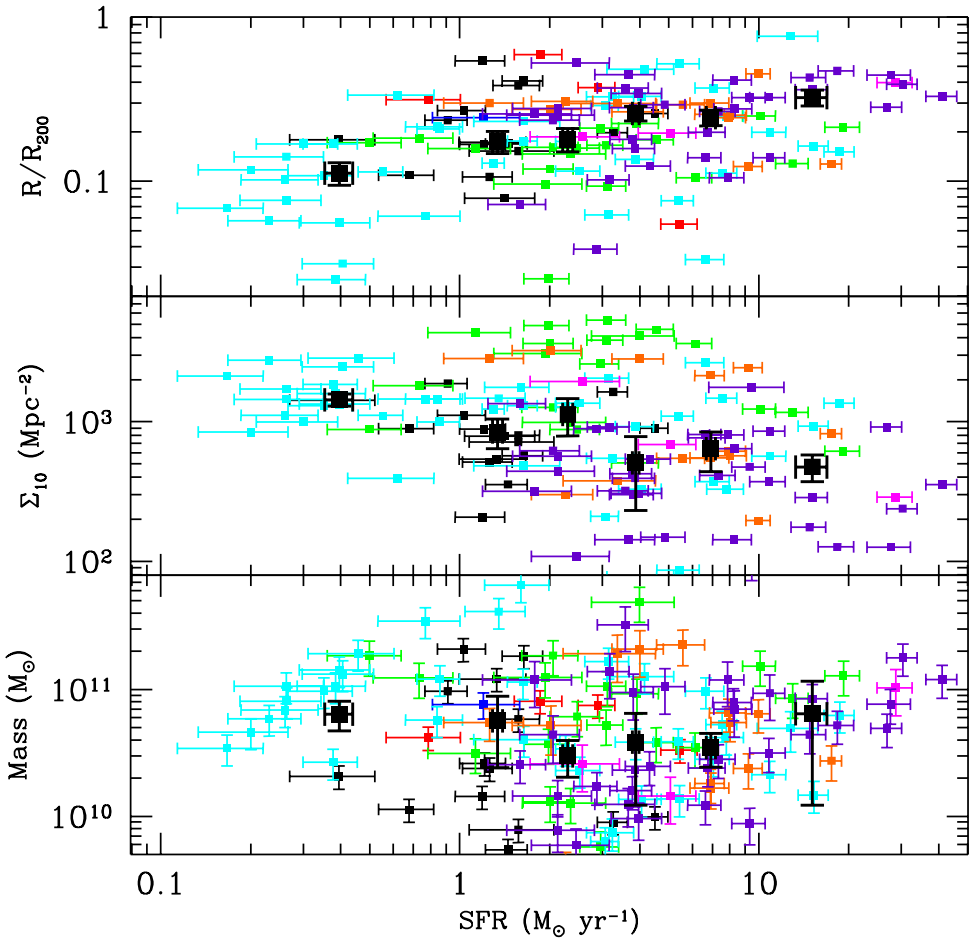

Fig. 4.—: Correlations of star formation with position in the cluster (top row), projected local density (middle row), and stellar mass (bottom row). Galaxies with no measurable star formation are neglected. Colors denote the different clusters in the sample: A3128 (*black*), A3125 (*red*), A644 (*blue*), A2104 (*green*), A1689 (*cyan*), A2163 (*magenta*), MS1008 (*orange*), AC114 (*violet*). Large black points show the median values of the galaxy sample after it has been binned by SFR. SFR shows strong correlations with both R/R_{200} and Σ_{10} ($r_S = +0.35$ and $r_S = -0.34$, respectively), but no correlation with M_*. Partial correlation coefficients derived from these data are listed in Table 4.

-0.03). This conflicts with Christlein & Zabludoff (2005), who reported a strong correlation of SFR with local substructure. However, δ requires a robust spectroscopic sample from which to measure local velocity dispersions. As a result, the substructure measurements for some of our clusters with less complete spectroscopy are probably unreliable. We repeat the test with A3128 and A3125, which have the most complete spectroscopy and are the only two clusters with significant substructure. The results are indistinguishable from the full cluster sample.

6.2. Mass–Radius Relation

In §6.1, we reported a strong correlation of SFR with R/R_{200} but no residual dependence of SFR on M_* or M_* on radius. This might indicate that M_* is independent of environment, as von der Linden et al. (2010) found. However, it might also mean that the SFR–R/R_{200} correlation is strong enough to eclipse any more subtle correlations that might appear among a sample composed entirely of SFGs. The galaxy sample examined in §6.1 includes only a few hundred galaxies, and the sample preferentially excludes the most massive galaxies, which tend not to show active star formation. As a result, §6.1 might show no correlation between M_* and R/R_{200}, even if the full cluster galaxy sample includes one. Christlein & Zabludoff (2005) found a strong partial correlation of mass with R/R_{200}. This correlation would be difficult to produce if BCGs alone produce a false correlation of M_* with R/R_{200}, as von der Linden et al. (2010) claim, because normal cluster galaxies are much more numerous than BCGs.

To test whether our data support the presence of a radial trend in M_*, we look for direct variations of M_* with R/R_{200} without regard to correlations with other variables. We first divide the galaxy sample into two samples with equal numbers of galaxies, and we apply a K-S test to check for a difference between their radial distributions. For this analysis, we include members of all 8 clusters, and we exclude BCGs as defined by von der Linden et al. (2007) from the sample. The results are shown in Figure 5a. The K-S test returns a probability $< 0.1\%$ that the high- and low-mass samples have the same radial distributions, so massive galaxies are preferentially found closer to the centers of their parent clusters, even in the absence of BCGs. We weight members of the main cluster sample by their completeness to determine the average mass as a function of radius. The average mass in a given bin is,

$$\langle M_* \rangle = \frac{\Sigma_{i=0}^{N} \left[w_i M_{*,i} \right]}{\Sigma_{i=0}^{N} \left[w_i \right]} \tag{7}$$

where N is the number of galaxies in the bin with $M_R < -20$. The w_i are the weights

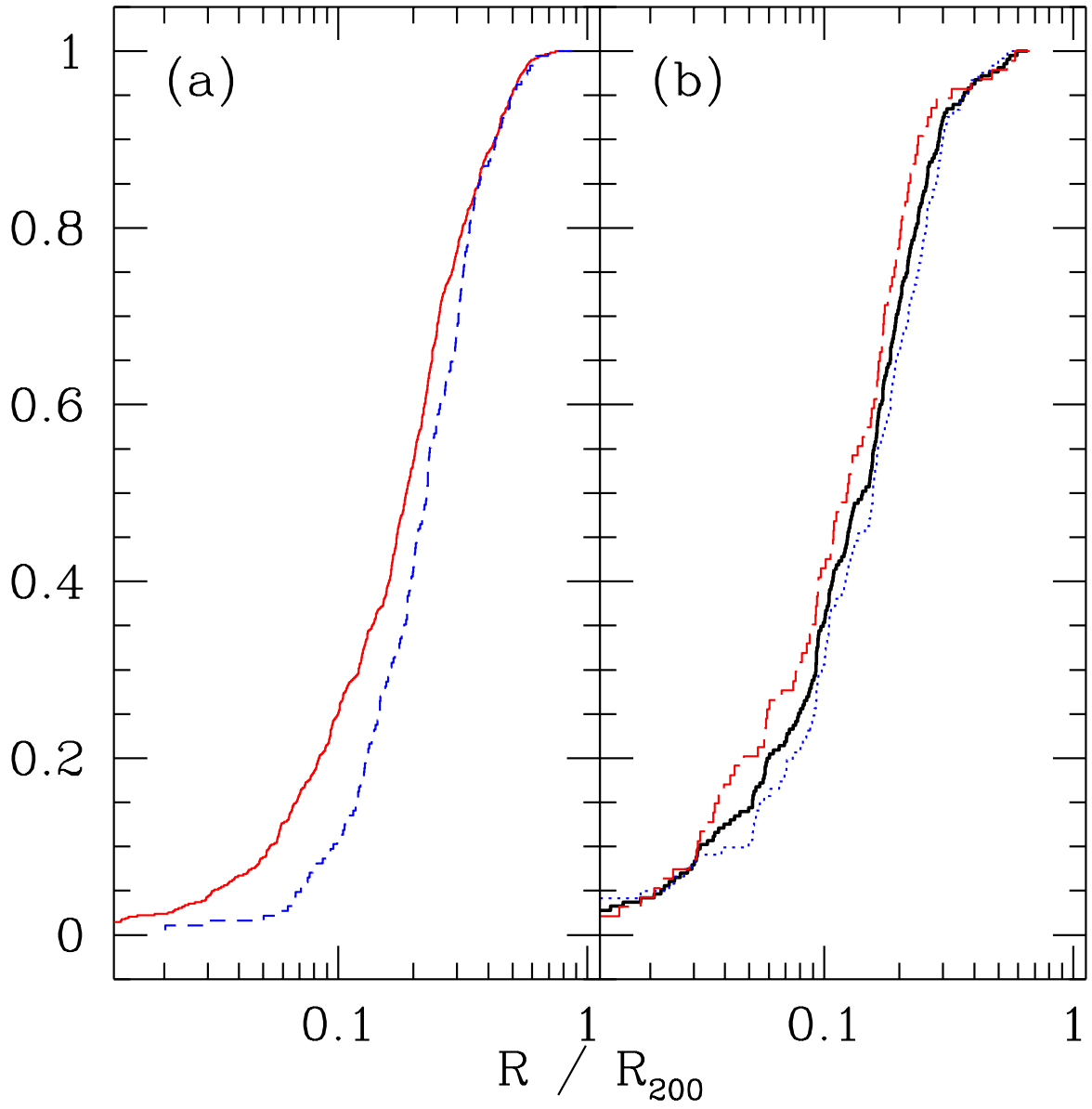

Fig. 5.—: Radial distributions of all cluster members scaled to R_{200}. Panel (a) compares the radial distributions of low-mass (*blue dashed*) and high-mass (*red solid*) galaxies, divided into two equally-sized subsamples at $M_{cut} = 3.9 \times 10^{10}\ M_{\odot}$. The two distributions differ at 99.9% confidence after we exclude BCGs as defined by von der Linden et al. (2007). Panel (b) compares the radial distributions of galaxies with (*blue dotted*) and without (*red dashed*) an $8\mu m$ flux excess to the distribution of all galaxies with $8\mu m$ detections (*heavy black*). The distribution of galaxies with no measurable excess shows a marginal difference compared to the distribution of all cluster members (95% confidence).

derived from Eq. 4. Figure 6 shows the resulting average masses as a function of radius.

The innermost radial bin Figure 6 shows a strong excess compared to the other bins, and the second bin hints at an excess. We fit a power law to the six outer radial bins in Figure 6 (solid line) to measure the strength of the mass excess in these bins and to determine why our results differ from von der Linden et al. (2010). The slight increase of $\langle M_* \rangle$ with R/R_{200} beyond $R \approx 0.1R_{200}$ is consistent with the tendency of massive galaxies to be accreted more recently than less massive galaxies and for recently accreted galaxies to lie further out in the cluster (De Lucia et al. 2011). Alternatively, galaxies presently near the center of the cluster spend more time near the cluster center, on average, than galaxies farther away. Therefore, they are subject to stronger tidal forces from the cluster potential and will lose more of their mass (Merritt 1983, 1984; Natarajan et al. 1998). The large uncertainties on the fit preclude any attempt to distinguish between these scenarios.

Figure 6 shows that the average masses of galaxies near the cluster center show an excess compared to their counterparts further out in the cluster. The innermost radial bin in Figure 6 differs from the best fit model by 2.8σ, and the mass excess in the second radial bin is significant at 1.8σ. This indicates that the cluster core ($R \lesssim 0.05R_{200}$) tends to host more massive galaxies than the outer regions, even if we neglect BCGs. Mass segregation among cluster galaxies can be introduced as the cluster relaxes to virial equilibrium. The dynamical relaxation timescale in the inner mass bin for a cluster at $z = 0.15$ with $\sigma = 1200\ km\ s^{-1}$ is approximately 300 Myr, so the core of a typical cluster in our sample should be dynamically relaxed. For the same "typical" cluster, the crossing time for the sphere defined by $R \leq 0.4R_{200}$ is approximately 900 Myr. This crossing time implies a dynamical relaxation time of 7 Gyr, which is longer than the age of a cluster at $z = 0.15$ that "assembled" at $z = 1$ (5.8 Gyr), so the sphere with $R \leq 0.4R_{200}$ has not yet had time to relax.

Finally, Figure 6 suggests a reason for our disagreement with von der Linden et al. (2010). The signal comes primarily inside $0.05R_{200}$, which corresponds to $\sim 1\farcm5$ at the median redshift of the von der Linden et al. (2010) sample ($z \approx 0.8$). Due to SDSS fiber collisions, only a few galaxies inside $0.05R_{200}$ will have redshifts in each cluster. This shifts the median of the innermost radial bin in the von der Linden et al. (2010) sample to $\sim 0.08R_{200}$. This is comparable to the second radial bin in Figure 6. If this was our innermost bin, we would not find any dependence of M_* on R/R_{200}, so the disagreement between our results and von der Linden et al. (2010) likely result from fiber collisions in SDSS.

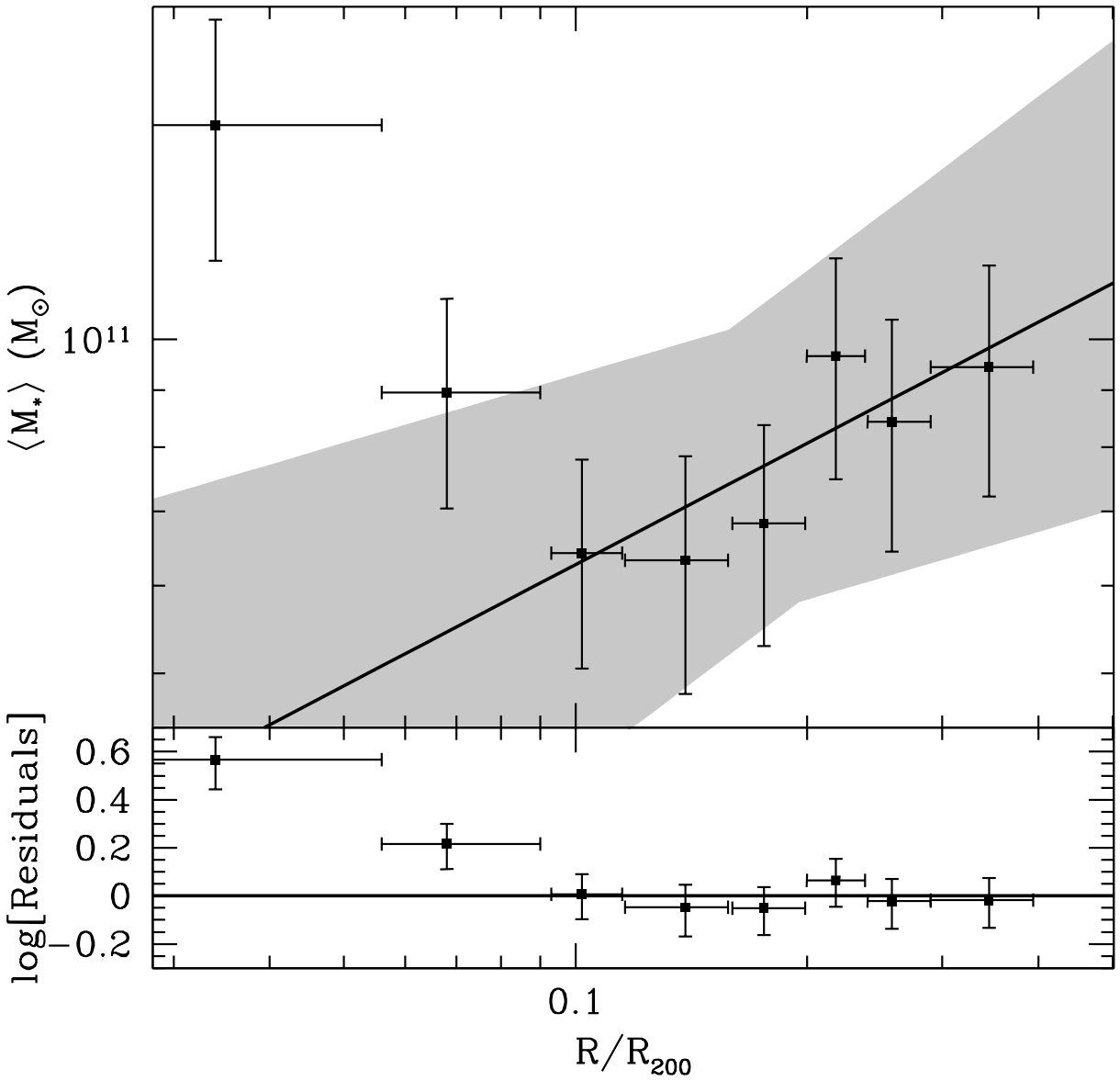

Fig. 6.—: Average stellar mass for galaxies in the stacked cluster sample as a function of radius. Brightest cluster galaxies are excluded from the fit because of their unusually large stellar masses and SFRs compared to other galaxies near the centers of clusters. The heavy line indicates the best-fit power-law to the 6 outer bins. The two innermost radial bins were excluded from the fit based on their large excesses. This resulted in a reduction in total χ^2 from 9.1 to 1.0. The best fit yields $M_* \propto \left[R/R_{200}\right]^{0.4\pm0.2}$, and the shaded region indicates the 68% confidence interval to the fit. The residuals are shown in the lower panel.

6.3. Environmental Dependence of SFR

In Paper I, we examined the R/R_{200} distributions of AGNs and found no significant difference between the positions of AGNs and normal cluster members. The lack of radial dependence among AGNs could due to the small sample size, it could indicate a weak dependence of the amount of cold gas on R/R_{200}, or it might mean that AGN fueling is poorly correlated with the total cold gas reservoir of its host galaxy. To test these hypotheses, we define a sample of galaxies with $8\mu m$ flux excesses as those galaxies whose measured $8\mu m$ flux exceeds the flux expected from a passively evolving galaxy matched in M_K at more than 2σ. Figure 5b compares the radial distributions of galaxies with and without an $8\mu m$ excess. These objects include both SFGs and AGNs. We again excluded BCGs from these samples. The radial distribution of galaxies with $8\mu m$ excesses is indistinguishable from the merged sample, but galaxies without an excess are located closer to the centers of their host clusters than the average cluster galaxy at 95% confidence.

The dependence of dust emission on R/R_{200} shown in Figure 5b is consistent with the established dependence of SFR on position within galaxy clusters (Kodama & Bower 2001; Balogh et al. 2004; Christlein & Zabludoff 2005; Hansen et al. 2009; von der Linden et al. 2010) and with our results in §6.1. One way to test the origin of this effect, and by extension the SFR–density and SFR–radius relations, is to measure the average SFR as a function of radius. We weight individual SFGs by their total completeness (Eq. 6) and bin them in radius to determine $\langle SFR \rangle$:

$$\langle SFR \rangle = \frac{\Sigma_{i=0}^{N_{SF}} \left[w_{SF,i} SFR \right]}{\Sigma_{j=0}^{N_{gal}} \left[w_j \right]} \tag{8}$$

where $w_{SF,i}$ and w_j are the weights for SFGs and all galaxies, respectively. For this calculation, we define SFGs as all galaxies with $SFR \geq 3\ M_\odot\ yr^{-1}$. This guarantees that we are not subject to biases due to variable sensitivities across the cluster fields.

We fit a power law to $\langle SFR \rangle$ as a function of R/R_{200} and find,

$$\log_{10}\left[SFR\right] = (1.3 \pm 0.7) \log_{10}\left[R/R_{200}\right] + (1.3 \pm 0.6) \tag{9}$$

where SFR is the average in each radial bin. The fit yields $\chi^2_\nu = 1.2$ and is shown by the solid line on the upper panel with the 1σ uncertainty given by the grey region. The red line shows the gradient predicted by the gas starvation model of Book & Benson (2010), normalized to minimize the χ^2 between the model and the observed SFRs. The model predicts the average SFR for all non-BCG cluster members at $z = 0$, so the higher redshift of the cluster galaxies in Figure 7 might explain the shift in $\langle SFR \rangle$ between the observations and the model. However, even after we adjust the normalization of the model, it remains a poor

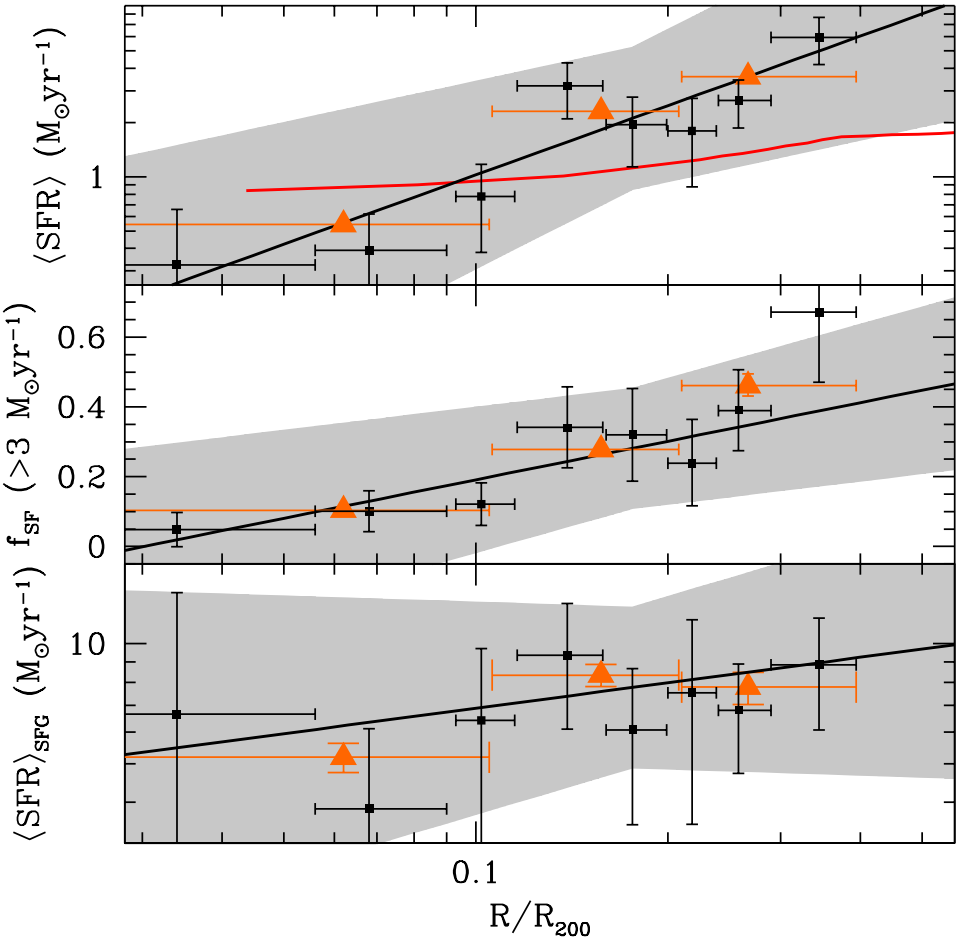

Fig. 7.—: Average star formation in the stacked cluster sample as a function of position. Each panel shows two different binning schemes: fine (*black squares*) and coarse (*orange triangles*) for the same galaxy samples. The *top panel* shows average SFR among all galaxies. The solid line indicates the best-fit power law to the data $\left(SFR \propto \left[R/R_{200}\right]^{1.3\pm0.7}\right)$, and the *red line* shows the gas starvation model of Book & Benson (2010), normalized to match the observed SFRs. The shaded region indicates the 1σ confidence interval to the fit. The *middle panel* shows the fraction of SFGs ($SFR > 3\ M_\odot\ yr^{-1}$) as a function of position, with the best fit $\left(f_{SF} \propto [R/R_{200}]^{0.4\pm0.2}\right)$ shown by the line and the 1σ confidence interval shown by the shaded region. The *bottom panel* shows the averaged SFR among SFGs ($\langle SFR\rangle_{SFG}$) versus R/R_{200}. Galaxies with $R/R_{200} \lesssim 0.1$ have lower $\langle SFR\rangle_{SFG}$ than galaxies outside $0.1R_{200}$ at $> 99.9\%$ confidence.

fit to the data ($\chi^2_\nu = 3.2$), but the re-normalized model is marginally consistent with the best-fit power law within the large statistical uncertainty on the fit.

Despite the significant uncertainty in the power law fit to the SFR–radius relation, Figure 7 clearly demonstrates higher $\langle SFR \rangle$ toward the outer regions of the stacked cluster sample. This mirrors the trend found via partial correlation analysis in §6.1, which is significant at >99.9% confidence. A similar trend appears in $\langle sSFR \rangle$ as a function of radius, which yields $\langle sSFR \rangle \propto (R/R_{200})^{1.0\pm0.6}$. To interpret Eq. 9 in detail, we need a model that better agrees with the observations than the Book & Benson (2010) model and that accounts for projection effects, the distribution of orbits followed by cluster members, and the effect of different environmental processes.

The RPS scenario makes at least one clear, qualitative prediction that we can use to evaluate its impact without a detailed model. Because RPS operates quickly compared to the cluster crossing time, the radial variation in $\langle SFR \rangle$ should be caused by variations in the fraction of SFGs (f_{SF}), and there should be little change in the SFRs of individual galaxies. The middle panel of Figure 7 shows that f_{SF} declines strongly near the cluster center, which is consistent with RPS. We also see lower $\langle SFR \rangle$ among SFGs with $R \lesssim 0.1\ R_{200}$ compared to SFGs with $R > 0.1R_{200}$ (bottom panel). This difference is formally significant at $> 99.9\%$ confidence, so SFGs with $R \lesssim 0.1R_{200}$ experience a clear reduction in their SFRs as they transition to passive evolution. However, a fit to $\langle SFR \rangle_{SFG}$ versus R/R_{200} shows no significant trend, so the reduction in SFR at $R \lesssim 0.1R_{200}$ may be a sharp transition rather than a gradual decline. The time to cross this region is approximately 100 Myr, which is consistent with the hypothesis that the apparent break is due to the influence of RPS. The onset of this break, however, occurs much closer to the cluster center than is usually expected ($\sim 0.5R_{200}$; Treu et al. 2003).

The small region over which RPS has the strongest effect might explain the absence of the correlation between M_* and SFR that is expected under the RPS scenario. The most massive galaxies, which are best able to retain their gas, are preferentially found at $R \lesssim 0.1R_{200}$. These galaxies therefore experience stronger ram pressure than typical, less massive cluster members, and their ability to retain their gas is cancelled by the increased stripping they experience.

6.4. TIR Luminosity Function

Another probe of the impact of environment on star formation is the TIR luminosity function (LF). The TIR LF is sensitive to the frequency of star formation in clusters and

the rapidity with which it is quenched; this provides a strong empirical constraint on the types of processes that mediate the interaction between individual galaxies and the cluster environment. For example, Bai et al. (2009) found similar shapes (α and L^*) of the TIR LFs in the galaxy clusters that they measure compared to the field galaxy TIR LF. They argue that this similarity requires truncation of star formation on short timescales compared to the lifetime of star formation in individual galaxies. Such rapid transitions are inconsistent with processes like gas starvation and galaxy harassment.

To evaluate the conclusion that RPS dominates the evolution of star formation in galaxy cluster members, we will examine the TIR LFs of the clusters in our main cluster sample. We construct the LF as described in §5.2, and the results appear in Figure 8. The main cluster sample contains only 5 clusters, which prevents construction of subsamples that have different masses and similar redshifts. Therefore, we cannot reliably identify effects that are strongly dependent on cluster mass.

The dashed vertical line in Figure 8 marks the expected L_{TIR} of a galaxy with the Assef et al. (2010) spiral SED and $M_R = -20$. This marks the approximate TIR completeness limit imposed by the requirement that $M_R \leq -20$. We call this limit L_{TIR}^{thresh}. This limit is representative only, and Figure 8 includes many cluster members that have $M_R \leq -20$ and $L_{TIR} < L_{TIR}^{thresh}$. This is expected because cluster galaxies have lower $\langle sSFR \rangle$ than the field galaxies used to construct the Assef et al. (2010) templates. In fact, 65% of galaxies with $M_R < -20$ mag and measurable ($> 3\sigma$) MIR emission are less luminous than L_{TIR}^{thresh}. This means that L_{TIR}^{thresh} is robust, and the true limit is lower than the nominal value established from the spiral galaxy template. To predict the true L_{TIR}^{thresh}, we would need a model for the truncation of star formation in clusters, which is exactly what we want to measure. To be conservative, we restrict our fits to use only bins more luminous than L_{TIR}^{thresh}. Above this limit, we can be confident that the weights given by Eq. 6 will correct to the full galaxy population.

Like Bai et al. (2009), we find that the individual clusters in Figure 8 have luminosity functions that closely resemble the field galaxy LF at their respective redshifts. This agreement occurs despite the disagreement between the field galaxy LF and the combed cluster sample (Figure 9). While it is possible that the field galaxy LF at the median redshift of the cluster provides a poor estimate of L_{TIR}^* among galaxies that fall into clusters, any effects of preprocessing in the large-scale structure around the cluster should appear in Figure 8. A better explanation appears to be that the improved statistics in the combined cluster sample illuminate a discrepancy that is not visible in the individual clusters due to larger observational uncertainties.

At least some of the variation between the IR LFs observed in different clusters may

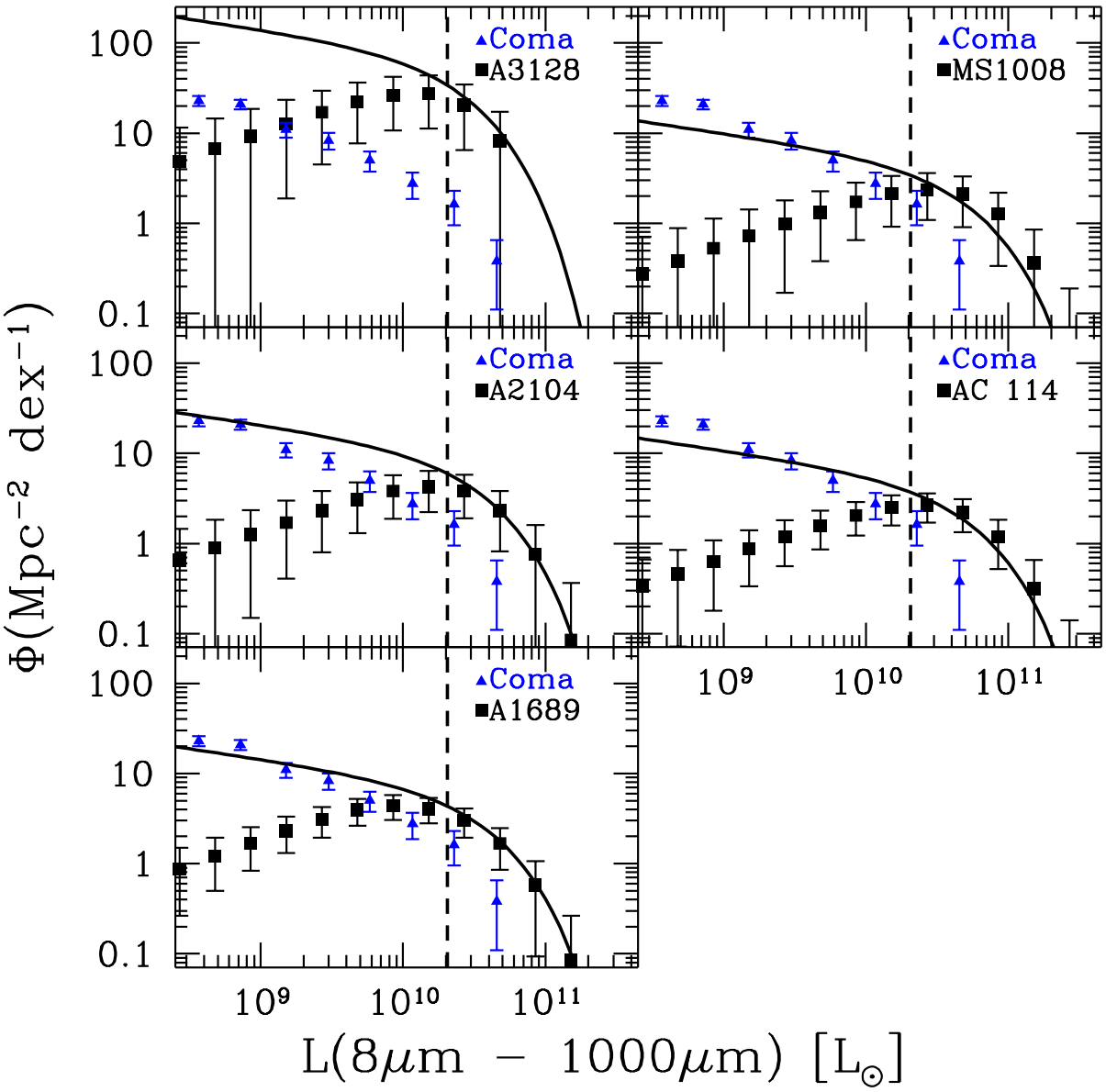

Fig. 8.—: Total infrared (TIR) luminosity functions for each of the 5 clusters in the main sample. Input galaxies are restricted to $M_R < -20$ and $R < 0.4R_{200}$. The Coma cluster LF (*blue triangles*; Bai et al. 2009) is shown for reference. The *solid black lines* on each panel show the field galaxy TIR LF of Pérez-González et al. (2005) shifted to the redshift of the cluster and normalized to match the observed LF above our nominal completeness limit of $2.1 \times 10^{10} L_\odot$ (vertical, dashed line), which is the approximate L_{TIR} expected for a normal, spiral galaxy with $M_R = 20$ mag. This indicates the expected distribution of SFRs among field galaxies that enter the cluster. The *dashed lines* mark the completeness limit imposed by the requirement $M_R < -20$. Some variation between individual clusters is apparent at the highest luminosities.

be caused by systematic uncertainties in the completeness corrections. We can only apply completeness corrections in regions of the clusters where we have both spectra and MIR photometry, so azimuthal asymmetry may be important. The LF of the stacked cluster sample averages over several selection regions, so it is less subject to this uncertainty.

We constructed the best-fit Schechter functions to both the Coma cluster and the stacked cluster shown in Figure 9. The Schechter function has the form,

$$\Phi(L) = \frac{\Phi^*}{L_*}\left[\frac{L}{L_*}\right]^{\alpha} e^{-L/L_*} \tag{10}$$

where $\Phi(L)$ gives the projected surface density of sources at TIR luminosity L, and α and L_* are the usual Schechter function parameters. We fixed $\alpha = -1.41$ in the fit to the cluster LF, which is the best-fit value for the Coma LF (Bai et al. 2006). Le Floc'h et al. (2005) suggest that the faint end of the LF cannot evolve much with redshift for $z \lesssim 1$, so the faint end of the LF in the Coma cluster is likely to provide a good estimate of α in all galaxy clusters. The best fit to the stacked main sample has $L_* = (6.6 \pm 1.1) \times 10^{10} L_\odot$.

If clusters rapidly shut off star formation in galaxies that fall in from the field, as Bai et al. (2009) conclude, then only galaxies that have recently become cluster members will have measurable star formation, and the TIR LF of a cluster should have L^* and α similar to the field galaxy LF at the same redshift. Therefore, we want to compare L_* to the field galaxy LF at the median redshift of the combined galaxy sample, $z_{med} = 0.24$. Le Floc'h et al. (2005) found that the field galaxy LF evolves as $L_* \propto (1+z)^n$, where $n = 3.2^{+0.7}_{-0.6}$. Pérez-González et al. (2005) studied the $12\mu m$ LFs of field galaxies from $z = 0$ to $z = 3$ and found that the field galaxy LF at $z = 0.1$ has $L^*_{12\mu m} = 4.1 \pm 1.3 \times 10^9 L_\odot$ and $\alpha = 1.23 \pm 0.07$. We use the prescription of Takeuchi et al. (2005) to convert their L^* to a TIR luminosity, which yields $L^*_{TIR} = 2.3 \times 10^{10} L_\odot$ at $z = 0.1$. We determine the field galaxy LF at the median redshift of the stacked cluster sample ($z_{med} = 0.211$) with the results of Le Floc'h et al. (2005) and fit the normalization of the LF to the observed cluster galaxy LF. The result is shown as the blue, dashed line in Figure 9. The quality of the fit ($\chi^2 = 4.7$) is considerably poorer than the fit shown by the heavy, black line ($\chi^2 = 0.5$), which uses α from the Coma cluster and fits for L^*_{TIR} and ϕ^*. While the absolute χ^2 values cannot be used to evaluate the quality of the fits due to the presence of correlated errors in adjacent bins, the Coma-based LF improves the quality of the fit by $\Delta\chi^2 = 4.2$ with only 1 additional degree of freedom.

Bai et al. (2009) found that the luminous ends of the TIR LFs of the Coma cluster and A3266 have similar shapes and that the L^*_{TIR} for these clusters are indistinguishable from the field galaxy LF. The similarity between the stacked cluster LF and the redshifted field galaxy LF for $L_{TIR} > 4 \times 10^{10} L_\odot$ is consistent with the conclusions of Bai et al. (2009). They

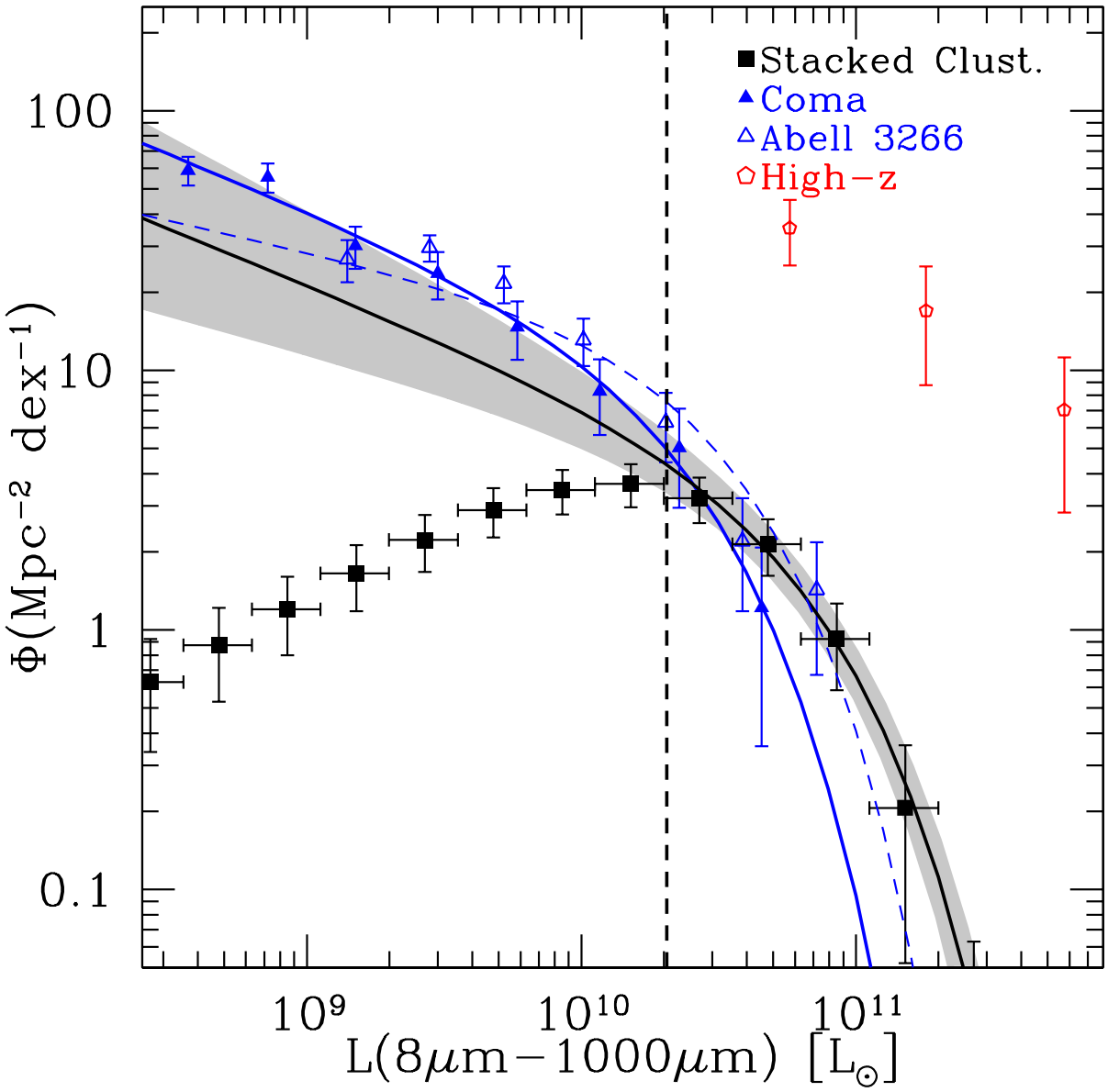

Fig. 9.—: TIR LF of the stacked cluster sample (*filled squares*) compared to the LFs derived by Bai et al. (2009) for Coma (*filled triangles*) and Abell 3266 (*open triangles*). The solid lines show the best fit LFs for the stacked sample (*black*) and for Coma (*blue*), and the shaded region shows the 68% confidence interval around the best fit to the stacked cluster LF. The *dashed line* shows the field galaxy LF of Pérez-González et al. (2005), and we have employed the prescription of Le Floc'h et al. (2005) to correct the LF to the median redshift of the combined cluster sample. The field galaxy LF is normalized to best match the observed LF above the nominal completeness limit. The average LF determined by Bai et al. (2009) from two high-z clusters (MS 1054-03 and RX J0152, *red pentagons*) is shown for comparison.

argue that the similar LF shapes in clusters and in the field suggests that gas starvation is not a plausible mechanism to end star formation among cluster member galaxies. Because gas starvation operates slowly ($\sim$ Gyr timescales), they conclude, it should produce many galaxies in the transition phase between SFGs and passive evolution. They found no such transition population. However, the combined cluster LF shown in Figure 9 displays a 4σ deficit of galaxies with moderate SFRs ($SFR \approx 5\ M_\odot\ yr^{-1}$) compared to the expectation from the field LF. This largely drives our conclusion that an unmodified field galaxy LF does not provide a good description of the SFG population in the merged cluster sample. The disagreement between the field and cluster galaxy LFs could indicate the presence of a transition population. It is possible that the discrepancy results instead from some selection effect not accounted for in our completeness estimates. The most obvious culprit for such an effect is some residual dependence of spectroscopic member identification on color that we have not been able to identify from the data.

As a test for radial gradients in the population of transition SFGs, we binned the galaxies in the main cluster sample into three radial bins with equal numbers of galaxies. The TIR LFs for the radial subsamples are shown in Figure 10. The L^*_{TIR} increases slightly from the innermost to outermost radial bins, but this increase is not statistically significant. This marginal decrease in L^*_{TIR} in the innermost radial bin is qualitatively similar to the results of Bai et al. (2009), who also examined the radial dependence of the TIR LF with a very similar binning scheme. However, the fractional change in L^*_{TIR} in the Coma cluster is much larger than observed in Figure 10. The increase in $\langle SFR \rangle_{SFG}$ seen in Figure 7 in the same radial bins does not appear to affect L^*_{TIR}. This indicates that the change in $\langle SFR \rangle_{SFG}$ is driven by the frequency of galaxies with $SFR \approx 3\ M_\odot\ yr^{-1}$.

6.5. Substructure and Preprocessing

Von der Linden et al. (2010) found a trend toward increased $\langle SFR \rangle$ at larger R/R_{200} that extended out to at least $2R_{200}$. They concluded that preprocessing in groups contributes significantly to the SFR–density relation. Our observations do not extend past $R = 0.4R_{200}$, so it is impossible to measure preprocessing directly, but A3128 shows significant substructure, so we can compare it to the smooth clusters in the sample to probe how the presence of substructure influences SFRs in clusters. This allows us to indirectly test the impact of group scale environments on SFGs, because coherent substructures in clusters should correspond to recently-accreted groups.

Before we can compare the integrated SFRs in different clusters, we must first correct for the different numbers of galaxies in each cluster. The sSFR naturally accounts for this

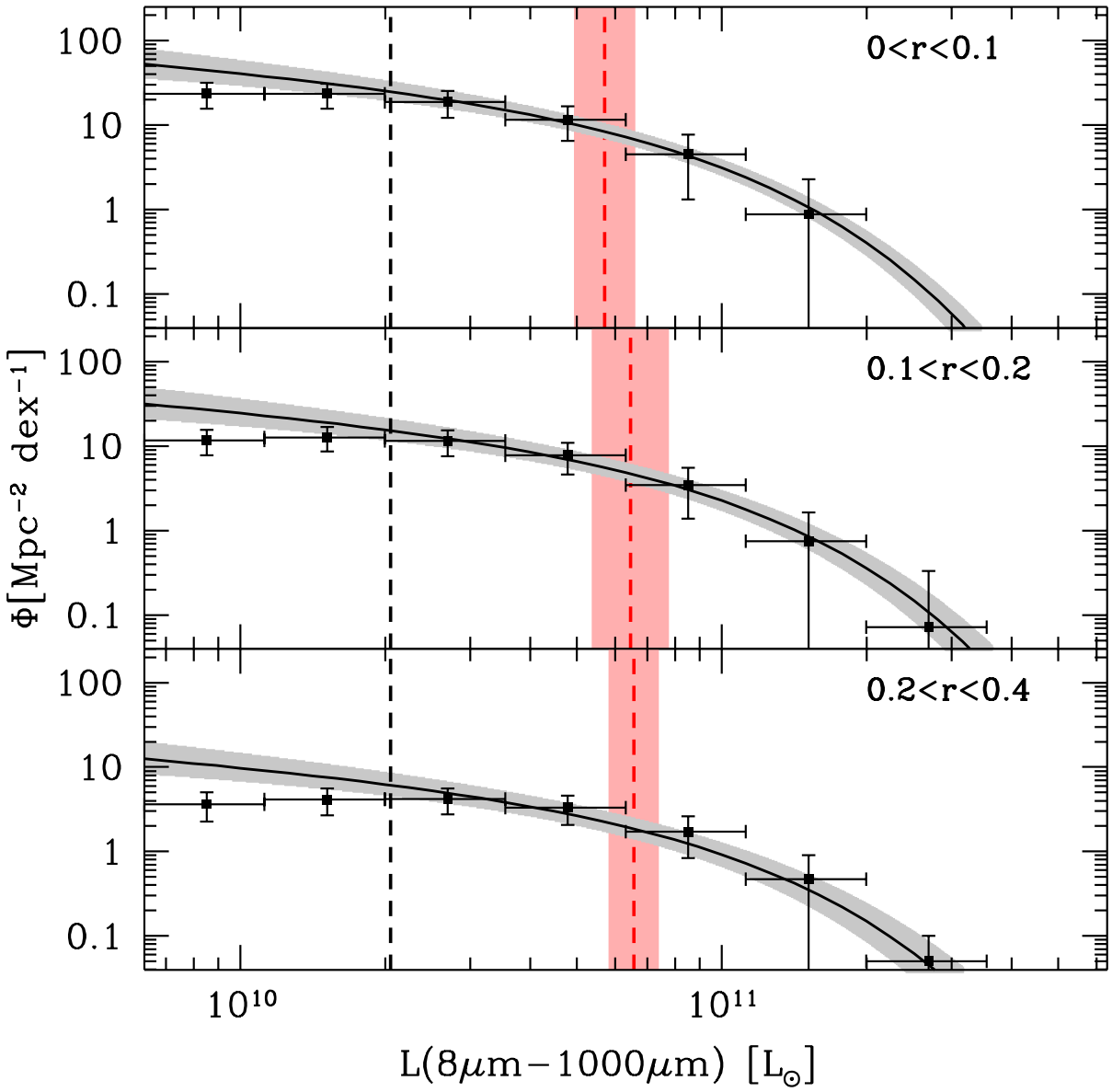

Fig. 10.—: TIR LF divided into radial bins with equal numbers of galaxies. Each panel is labeled with the range of radii that contribute to the LF, where $r = R/R_{200}$. The solid lines show the best-fit Schechter function to the LF in each radial bin, and the shaded regions show the uncertainties on the fit. The fits are constructed from the bin more luminous than the completeness limit (*dashed line*), which is set by the expected L_{TIR} for the Assef et al. (2010) spiral galaxy template at $M_R = -20$ mag. The *red, dashed lines* on each panel show the best-fit L^*_{TIR}, and its 1σ confidence interval is given by the shaded region. The three LFs hint at an increase in L^*_{TIR} analogous to the increase in $\langle SFR \rangle_{SFG}$ seen in Figure 7, but this increase is not statistically significant.

variation, and it is therefore a better parameter to compare integrated SFRs between clusters. We employ a method analogous to Eq. 8 to calculate the $\langle sSFR \rangle$ and compare A3128, which shows significant substructure, to the other clusters in the main sample. We find $\langle sSFR \rangle = 9.0^{+1.1}_{-1.2} \times 10^{-12}\ yr^{-1}$ and $\langle sSFR \rangle = 3.1^{+0.2}_{-0.2} \times 10^{-11}\ yr^{-1}$ in A3128 and in clusters without substructure, respectively. If we correct $\langle sSFR \rangle$ of A3128 to the mean redshift of the other clusters ($z = 0.241$), we find $\langle sSFR \rangle = 1.5^{+0.4}_{-0.4} \times 10^{-11}\ yr^{-1}$. This is still lower than the average of the clusters without substructure at $> 99.9\%$ significance.

The difference between A3128 and the other clusters might be a result of the structure in A3128, or A3128 might simply have an unusually low $\langle sSFR \rangle$ for its redshift. In the latter case, the observed difference would be a result of cosmic variance. We compared A3128 with the 4 individual clusters without substructure, and we found that A3128 has higher redshift-corrected $\langle sSFR \rangle$ than MS1008, which is approximately 50% more massive than A3128. However, the typical dispersion in f_{SF} among nearby clusters with $\sigma \gtrsim 800\ km\ s^{-1}$ is ~ 0.1 dex Poggianti et al. (2006), so to explain the observed deficit of $\langle sSFR \rangle$ in A3128 as cosmic variance would require a $\sim 3\sigma$ excursion. While cosmic variance provides a marginally plausible explanation for the deficit of $\langle sSFR \rangle$ in A3128, the presence of substructure appears to be the more likely cause. If the observed difference arose from groups that have recently fallen into the cluster, the excess sSFR in clusters without substructure would imply that the "average" group member is likely to have experienced preprocessing. This result may be absent from the partial correlation results (Table 4) because only $\sim 10\%$ of cluster members have ever been part of a large group (Berrier et al. 2009), and only former group members that have been accreted more recently than the e-folding timescale for star formation will show evidence of preprocessing.

The conclusions drawn from the measured SFRs of cluster members and from the integrated cluster properties depend strongly on the methods used to identify and correct for AGN. In Paper I, we noted that the IR and X-ray AGN selection techniques identify quite different samples. If we relied only on X-ray based AGN selection, as some authors do, the MIR luminosity contributed by unidentified AGN would lead to an overestimate in the integrated SFR of the cluster. For example, in A1689 we would overestimate the total SFR by 20%. Applied to all clusters simultaneously, this alternative method of AGN correction results in an inferred $\langle sSFR \rangle = 7.2^{+1.5}_{-1.3} \times 10^{-11}\ yr^{-1}$ among the clusters without measurable substructure but no measurable change in A3128. In this example, uncorrected AGN contamination would dominate the observed difference in $\langle sSFR \rangle$, and we would over-estimate the impact of preprocessing in the group environment.

6.6. MIR Butcher-Oemler Effect

The relative importance of gas starvation and RPS is also probed by the evolution in $\langle SFR \rangle$ as a function of cosmic time. The classic example of this is the Butcher-Oemler effect (Butcher & Oemler 1978). Haines et al. (2009) constructed an analogous measurement with SFRs measured via $\nu L_{\nu}(24\mu m)$ among the LoCuSS cluster galaxies. They employed a SFR threshold of 8.6 $M_{\odot}\ yr^{-1}$, and they found that $f_{SF} \propto (1+z)^{n}$ with $n = 5.7^{+2.1}_{-1.8}$. Figure 11 shows their fit to f_{SF} among the LoCuSS clusters as a function of redshift. The f_{SF} values for our clusters and for a higher redshift cluster sample measured by Saintonge et al. (2008) are superimposed. The 8 clusters in our sample, shown as the red triangles in Figure 11, are clearly consistent with the Haines et al. (2009) result within the uncertainties. However, the fit to the LoCuSS clusters systematically overpredicts f_{SF} in the Saintonge et al. (2008) clusters, despite the lower SFR threshold (5 $M_{\odot}\ yr^{-1}$) used by Saintonge et al. (2008).

In §6.5, we considered the impact of X-ray only AGN identification on the inferred $\langle sSFR \rangle$. This becomes a more important consideration at high-z, because the frequency of luminous AGNs increases dramatically (Martini et al. 2009). Figure 11 includes two points for each cluster in our sample. One shows f_{SF} with the IR AGN selection included (*filled triangles*), and the other shows f_{SF} that we would measure if we only knew about the X-ray selected AGNs (*open triangles*). The f_{SF} inferred from the X-ray only selection in AC114 differs by 1.6σ from the result when the full AGN sample is considered. This illustrates the contamination that X-ray only AGN identification can introduce to integrated SFRs. This contamination becomes more severe, and appears in other clusters, for SFR thresholds less than the fairly high value employed by Haines et al. (2009).

7. Discussion

In §6.1 and §6.3 we examined correlations between environment, SFR and M_{*}. We found a strong correlation of SFR with R/R_{200}, and we found evidence for a transition population of low-SFR galaxies near the cluster center. We interpret this population as evidence that galaxies in this region experience a rapid reduction in SFRs that initiates their transition from SFGs to passive galaxies. This interpretation was supported by a possible trend toward larger L^{*}_{TIR} farther out in the cluster (§6.4). We also found evidence for a concentration of massive galaxies near the cluster center (§6.2).

In this section, we consider the results of §6.3-6.5 in more detail and interpret them in the context of two competing mechanisms to end star formation in cluster galaxies: RPS and gas starvation (§7.1). We also briefly discuss the additional information that the Butcher-

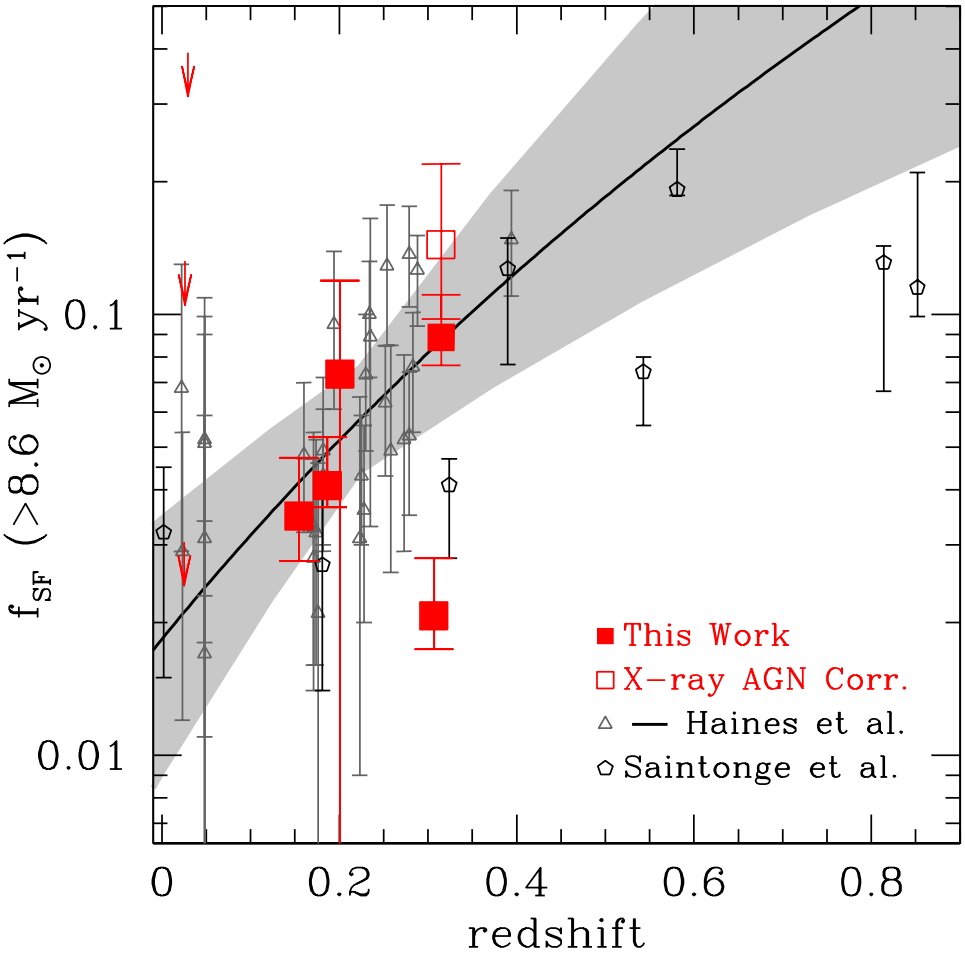

Fig. 11.—: Integrated fractions of SFGs (f_{SF}, $SFR > 8.6 M_{\odot} yr^{-1}$) in all 8 clusters as a function of redshift. *Filled red squares* mark the clusters in our sample for which we successfully measure f_{SF}, and *red arrows* mark the clusters for which we can produce only upper limits. *Open red squares* mark the f_{SF} that would be inferred from X-ray only AGN identifications. The filled and open squares overlap for all clusters except AC114. *Open grey triangles* indicate the LoCuSS clusters as reported by Haines et al. (2009), and *open black pentagons* mark the clusters measured by Saintonge et al. (2008). The solid line indicates the best-fit f_{SF}–z relation from Haines et al. (2009), and the shaded region shows the 1σ confidence interval for their fit ($f_{SF} \propto (1+z)^{5.7^{+1.8}_{-1.7}}$).

Oemler Effect can provide about the impact of the cluster environment on SFGs (§7.2).

7.1. Star Formation in Clusters

In §6, we examined several diagnostics for the impact of the cluster environment on star formation. These include partial correlation analysis, $\langle SFR \rangle$ and $\langle sSFR \rangle$ versus radius, and an examination of TIR LFs. The partial correlation results informed much of our subsequent analysis. One important result was the absence of a correlation between SFR and Σ_{10} once we control for R/R_{200}. This implies that interactions between individual galaxies have only a limited impact on star formation in cluster members. We conclude that the SFRs of cluster members are controlled by hydrodynamic interactions between galaxies and the ICM.

There is disagreement in the literature concerning the importance of different mechanisms to shut down star formation in clusters. For example, Simard et al. (2009) determined that evolution in cluster SFRs is controlled by galaxy-galaxy interactions because the growth in the fractions of early-type and passive galaxies track one another very closely in their sample. This contrasts sharply with our results in §6.1, which suggest that interactions with the ICM are the dominant factor. Of the hydrodynamic processes commonly considered (e.g. RPS and gas starvation), only RPS has been directly observed to work in nearby clusters (Kenney et al. 2004; Sivanandam et al. 2010). We therefore ask whether our observations are consistent with RPS alone or if an additional mechanism is required to explain the observations.

Treu et al. (2003) determined that RPS works effectively for Milky Way-like galaxies in a cluster with $M_{vir} = 8 \times 10^{14} M_{\odot}$ when $R < 0.5 R_{200}$. Our sample is restricted to projected $R < 0.4 R_{200}$, and their cluster mass is similar to the typical cluster in our sample ($M_{clust} \approx 5 \times 10^{14}\ M_{\odot}$), so RPS should act efficiently on most galaxies in our sample. Nevertheless, some of the obvious signatures of RPS do not appear: We found no residual correlation of SFR with M_* at fixed R/R_{200}, which is contrary to the prediction that RPS should affect low-mass galaxies more strongly. Furthermore, we found in §6.4 that the TIR LF of cluster galaxies is significantly better fit by a Schechter function with variable L^*_{TIR} and with the Coma cluster's faint-end slope than by a redshift-corrected field galaxy LF. This is inconsistent with the simplest prediction of RPS, which would suggest that the SFG population in clusters should be well-described by the field galaxy LF (Bai et al. 2006, 2009). To interpret this disagreement, we need to know whether it results from different faint-end slopes between the cluster population and the field, different L^*_{TIR}, or some combination of the two. This level of detail is impossible given the completeness limit in the present sample, so the implications of the poor agreement between the cluster and field SFG populations are

ambiguous. Finally, the best-fit power law to the SFR–radius relation is consistent—within very large observational uncertainties—with the predictions of Book & Benson (2010).

However, we also found evidence that RPS contributes significantly to the decline of SFRs among cluster galaxies. Figure 7 shows that the dependence of SFR on R/R_{200} is driven largely by a decline in f_{SF} toward the cluster center, and only a small fraction of the dependence is driven by decline in the SFRs of individual SFGs. This is more consistent with RPS than with gas starvation. Furthermore, the residual decline in $\langle SFR \rangle_{SFG}$ with R/R_{200} does not occur smoothly, but appears to set in rapidly at $R \approx 0.1R_{200}$. The crossing time for this region ($\sim 100\ Myr$) is consistent with RPS as the origin of the transition, but the small size of this region compared to the radius where RPS is theoretically expected to be important ($0.5\ R_{200}$) is surprising. This explanation is also difficult to reconcile with the decline in f_{SF}, which we attribute to RPS, across all radii.

To interpret Figures 7 and 10, we must consider projection effects and the influence of galaxy "backsplash". Projection effects will cause some galaxies at intrinsically large R/R_{200} to appear at small radii when the cluster is projected onto the plane of the sky. If we assume an R^{-2} density profile for galaxies and f_{SF} vs. R/R_{200} as determined by von der Linden et al. (2010), only $\sim 30\%$ of SFGs with projected $R < 0.3R_{200}$ actually fall within that region. This represents an upper limit, since the von der Linden et al. (2010) result also includes projection effects. Therefore, we cannot assume that SFGs at small R/R_{200} actually reside in the high density regions where RPS is most important. This suggests that SFGs that physically reside inside $0.1R_{200}$ have their SFRs reduced more drastically than implied by Figure 7.

"Backsplash" refers to galaxies on nearly radial orbits that pass through the dense central region of the cluster and return to large R/R_{200}. This effect can make radial gradients like the ones shown in Figure 7 particularly difficult to interpret, because even galaxies presently at large radii may have passed near the cluster center in the past. Gill et al. (2005) use N-body simulations to find that 50% of galaxies between 1-2R_{200} are backsplash galaxies, and 90% of these have been inside $0.5R_{200}$ at some point in the past. Pimbblet (2011) use mixture modeling with observations of real clusters from SDSS to infer that $60 \pm 6\%$ of galaxies at $R/R_{200} = 0.3$ are part of the backsplash population, so they were even deeper into the dense central region of the cluster at some point in the past. Galaxies on radial orbits in a cluster with an R^{-2} mass profile and a core radius of $0.05R_{200}$ spend only 4% of their time inside $0.1R_{200}$ and only 32% of their time inside $0.5R_{200}$. This model also implies that approximately half of the galaxies in a cluster with an age of 8 Gyr have previously passed through the cluster center. As a result, the dynamic nature of the cluster populations smears the dependence of star formation on projected radius relative to the

underlying, three-dimensional trends. This suggests that the projected trends shown in Figure 7 are lower limits to the true, three-dimensional trends.

The effects of projection are potentially just as important. We adopt the simple mass profile described above, which implies that $\sim 40\%$ of galaxies with projected $R < 0.1R_{200}$ actually reside outside $0.1R_{200}$. However, the trend in f_{SF} versus radius (Figure 7) implies that at least 67% of SFGs that appear with $R < 0.1R_{200}$ in projection are likely to have three-dimensional radii outside this limit, and 20% of SFGs with projected $R < 0.4R_{200}$ will lie outside this radius. The steep dependence of f_{SF} on radius therefore works to mitigate any radial trends among the SFG population, which would lead to the small dependence of $\langle SFR \rangle_{SFG}$ on R/R_{200}. This suggests that the sharp drop in $\langle SFR \rangle_{SFG}$ at projected radius $0.1R_{200}$ would be stronger if measured relative to physical radius.

An ideal way to account for both projection and backsplash in our observables is to compare our results to models that include these effects. This approach allows more reliable conclusions than simple, *ad hoc* arguments. Book & Benson (2010) developed a model for the removal of hot gas from galaxies by the ICM, which is the physical mechanism that drives gas starvation. Their "shocks" model predicts that galaxies that experience this process should show $SFR \propto (R/R_{200})^{\sim 0.6}$ between 0.1-0.4R_{200} (their Figure 3). This is consistent with our results in §6.3 ($\langle SFR \rangle \propto (R/R_{200})^{1.3 \pm 0.7}$). However, the model yields overall poor agreement with the data, even after we fit the normalization of the model to best match the observations. This contrasts with the results of Book & Benson (2010), who found that their model agrees well with the SFR–radius relation measured among the CNOC clusters (Balogh et al. 2000). The resolution of this conflict will require additional observations and more sophisticated theoretical models that provide predictions for competing processes.

The large statistical uncertainties on the measured SFR versus R/R_{200} preclude detailed comparisons between our observations and a model for either RPS or gas starvation, so we must rely on qualitative arguments. Figure 9 demonstrates that the field galaxy TIR LF at the median redshift of the combined cluster galaxy sample provides a poor match to the observed TIR LF, and this discrepancy is most pronounced among galaxies with the lowest SFRs. The bottom panel of Figure 7 also shows a sudden decrease in the SFRs of SFGs with projected radii $R < 0.1R_{200}$. The crossing time for this region is ~ 200 Myr, which suggests that RPS is responsible for this reduction. However, only 5% of SFGs in the cluster have $R < 0.1R_{200}$, so this reduction in the SFRs of SFGs near the cluster center cannot account for the discrepancy between the TIR LFs of cluster and field galaxies. There must also be an effect at larger radii that is not apparent in the present sample. The entire sample has $R < 0.5R_{200}$, so either RPS or gas starvation could plausibly cause the disagreement.

In contrast to our results, Bai et al. (2009) found that the TIR LFs of many clusters

are consistent with one another and with the field LF. They inferred that cluster galaxies only rarely occupy a transition phase between SFRs characteristic of field galaxies and complete passivity. From this, they determined that star formation in cluster galaxies must be truncated on short timescales compared to the lifetime of the cluster. Both we and Bai et al. (2006) find $\sim 1\sigma$ variations in the shape of the TIR LF in different R/R_{200} bins. The observed decreases in L^*_{TIR}, while not statistically significant, are consistent with the decline in $\langle SFR \rangle_{SFG}$ for $R < 0.1R_{200}$ (Figure 7). The latter result indicates that the high ICM density near cluster centers reduces SFRs in individual SFGs. The smooth decline in f_{SF} as a function of R/R_{200} suggests that this process eventually results in the end of star formation in these galaxies. Projection effects and backsplash will both influence the observed trends. Projection would cause us to mistake galaxies at large R/R_{200} for galaxies near the cluster center, while backsplash would move galaxies that had been processed near the cluster center back to the outskirts of the cluster. Both effects would cause the projected trends to appear weaker than the true, three-dimensional variations in the cluster. This suggests that the observed radial variations are real, and the trends with projected radius likely underestimate the intrinsic, three-dimensional trends.

We find lower $\langle SFR \rangle_{SFG}$ inside $0.1R_{200}$ compared to outside this radius. We also see hints of this change in the lower L^*_{TIR} near the cluster center compared to further out. The variation in the properties of SFGs implied by these measurements indicates a substantial change in the SFGs very close to the cluster center. The crossing time for the sphere with radius $0.1R_{200}$ is less than 200 Myr, which strongly favors RPS as an explanation. However, we also see indications for a deficit in the number of low-SFR cluster galaxies relative to the field population. Because only $\sim 5\%$ of SFGs have projected $R < 0.1R_{200}$, galaxies outside $0.1R_{200}$ must dominate the under-abundance of galaxies with $SFR \approx 3M_\odot\ yr^{-1}$.

We can determine whether RPS or gas starvation are more likely to be responsible for the deficit from the time required to make the transition. We find that 66% of SFGs with $M_R < -20$ mag have $L_{TIR} < L^{thresh}_{TIR}$, where L^{thresh}_{TIR} is the luminosity expected for a typical field spiral with $M_R = -20$. If 50% of field SFGs with the same M_R distribution had $L_{TIR} < L^{thresh}_{TIR}$, then 16% of cluster SFGs would be in transition. Combined with the gas consumption timescale of a typical spiral galaxy (2.4 Gyr; Bigiel et al. 2011), this implies a transition time of ~ 400 Myr. This timescale is approximately twice the dynamical time of an ordinary spiral galaxy. This timescale favors RPS as the dominant mechanism among the full cluster sample, because RPS implies that galaxies should remain in a transition phase for approximately their dynamical time while the cold ISM is stripped. However, the assumption that 50% of field SFGs in an M_R-matched sample would have $L_{TIR} < L^{thresh}_{TIR}$ is arbitrary. A comparison of the SFR–M_R relations in clusters and in the field is required to measure the transition time more precisely.

If star formation in most cluster galaxies ends as a result of RPS, post-starburst galaxies should be more frequent in clusters than in the field. This is a robust prediction of any scenario that results in a rapid transition of SFGs to passive evolution. Galaxies with K+A spectra, which are usually associated with post-starburst populations, should remain visible for $\sim$ 100 Myr to 1 Gyr. This is short compared to the cluster crossing time, so a large population of K+A galaxies relative to SFGs would be strong evidence that RPS plays an important role. Instead, Yan et al. (2009) report that galaxies with K+A spectra are less common in overdense environments like clusters than in the field at $z \approx 0.1$. They suggest that K+A galaxies appear at constant absolute density, and that this density corresponds to the group scale at $z \approx 0$. Dressler et al. (1999) instead found that the fraction of K+A galaxies is much higher in clusters than in the field, and von der Linden et al. (2010) found no dependence of the ratio of N_{K+A}/N_{SF} on R/R_{200}. The different methods used by these authors to select their K+A samples—Dressler et al. (1999) rely on [OII] to exclude SFGs, while Yan et al. (2009) use Hβ, and von der Linden et al. (2010) select galaxies with excess Balmer line absorption from their principal component analysis—may account for the apparent contradictions in these observational results.

Groups that have recently fallen into a cluster might appear as an excess in the substructure parameter (Dressler & Shectman 1988). In our sample only A3125 has a mass comparable to galaxy groups, and we have not considered that cluster in our analysis. Therefore, we cannot directly constrain the mechanism that drives SFR evolution in group members. However, we find that $\langle sSFR \rangle$ is higher among clusters with no substructure than in A3128, which is the only member of our main sample with significant substructure. This could indicate that galaxies that have recently been part of groups have experienced preprocessing, but it could also arise from cosmic variance. In a recent study of SDSS galaxy clusters, von der Linden et al. (2010) found a trend of SFR with radius that extended to $2R_{200}$. They concluded that preprocessing of galaxies before they become cluster members is likely to contribute significantly to the SFR–radius relation. Additional observations are required to determine if galaxy groups are responsible for the preprocessing or if other processes are required.

7.2. Evolution

In §6.6 we suggested that the evolution of star formation in clusters is sensitive to the mechanism(s) responsible for the appearance of the $z = 0$ SFR–density relation. In particular, the rate of evolution of f_{SF} is sensitive to the operation of the cluster environment on recently accreted field galaxies. Figure 11 shows the fraction of SFGs in clusters as

a function of redshift since $z \approx 0.8$ for the clusters in our sample (*red*) compared to the samples of Saintonge et al. (2008) and Haines et al. (2009).

We use measurements of f_{SF} versus z to estimate the time required for f_{SF} in clusters to decline by a factor of e compared to coeval field galaxies. The best-fit to the Haines et al. (2009) galaxies $\left(f_{SF} \propto (1+z)^m,\ m = 5.7^{+2.1}_{-1.8}\right)$ is shown as the black line in Figure 11, and it agrees well with the clusters in our sample. Le Floc'h et al. (2005) report that the field galaxy LF evolves as $L^*_{TIR}(z) \propto (1+z)^n$, where $n = 3.2^{+0.7}_{-0.2}$. Approximately 70% of cluster member galaxies at $z = 0$ never had a massive companion before they entered the cluster environment (Berrier et al. 2009), so we can assume that galaxies that fall into the cluster have the same LF as field galaxies. The threshold we use to identify SFGs ($SFR > 8.6\ M_\odot\ yr^{-1}$) is larger than the SFR that corresponds to L^*_{TIR} ($4\ M_\odot\ yr^{-1}$), so we assume that f_{SF} among field galaxies has the same redshift dependence as L^*_{TIR}. With this assumption, we can measure the relative change in f_{SF} as a function of redshift and determine how the cluster environment induces SFGs to turn passive. The ratio of $f_{SF,clust}$ to $f_{SF,field}$ has undergone approximately 1.7 ± 1.2 e-foldings since $z = 1$. The elapsed time over this redshift interval is 7.7 Gyr, so the e-folding time for $f_{SF,clust}/f_{SF,field}$ is $4.6^{+10.6}_{-1.8}$ Gyr.

The e-folding time of f_{SF} does not correspond directly to the truncation time for star formation in individual cluster members. New SFGs constantly fall into the cluster from the field, and this results in a longer timescale for $f_{SF,clust}/f_{sf,field}$ to decline than for SFRs to decline in individual galaxies. The rate at which SFGs fall into the cluster combines with the timescale for the conversion of individual SFGs to passive evolution to determine how rapidly $f_{SF,clust}/f_{SF,field}$ changes. The timescale for this change is long compared to the gas exhaustion time in typical spiral galaxies (2.4 Gyr, Bigiel et al. 2011), but this does not necessarily indicate that the timescale for the evolution of individual SFGs is similarly long. If the timescale for evolution of individual SFGs is indeed long, it would favor gas starvation over RPS as the primary mechanism to end star formation in cluster galaxies.

In addition to the degeneracy between changes in rates of infall and the timescale for individual SFGs to stop forming stars, the measured timescale for $f_{SF,clust}/f_{SF,field}$ to evolve includes significant observational uncertainty. The Haines et al. (2009) best-fit overpredicts f_{SF} among the high-z clusters, despite the higher SFR threshold employed by Haines et al. (2009), so it underestimates the timescale over which $f_{SF,clust}/f_{SF,field}$ evolves. Additional observations are required to correct this bias. A measurement of f_{SF} versus z with a longer redshift baseline and consistent identification of SFGs will appear in our next paper.

8. Summary and Conclusions

We have used visible to MIR observations of 8 low-z galaxy clusters to constrain the impact of the cluster environment on star formation. We examined the relationship between star formation and environment among cluster members and found a strong correlation, with $\langle SFR \rangle \propto (R/R_{200})^{1.3\pm0.7}$, and this simple power law provides a good match to the data. Book & Benson (2010) model the impact of gas starvation on star formation. Their model is marginally consistent with the power-law that best fits the observed SFR–radius relation, but it is a poor fit to the data themselves. The $\langle SFR \rangle$–R/R_{200} relation is dominated by a decline in the fraction of SFGs toward the cluster center, but we also find lower $\langle SFR \rangle$ among SFGs with projected $R < 0.1R_{200}$. The dominance of the decline in f_{SF} and the short crossing time of a sphere with radius $0.1R_{200}$ both suggest that RPS contributes significantly to the observed trend in SFR with R/R_{200}. The TIR LFs hint at a shift toward lower L^*_{TIR} near the cluster center, which is consistent with the observed decline in $\langle SFR \rangle$, but this shift is not statistically significant. Projections effects and backsplash both work to weaken the observed trends relative to the intrinsic variation in three dimensions, which can hide the steep gradients that would be expected from RPS.

We also examined the relationship between R/R_{200} and stellar mass in cluster galaxies. We found that galaxies with $R \lesssim 0.1R_{200}$ show larger $\langle M_* \rangle$ than galaxies farther out in the cluster, even after we have eliminated BCGs from our sample. This excess is significant at $\sim 3.5\sigma$, and projection effects are also expected to weaken the observed trend relative to the intrinsic, three-dimensional variation, so we conclude that it is robust. Von der Linden et al. (2010) found no such excess once they had removed BCGs, so our result conflicts with theirs. This difference may result from the SDSS fiber collisions. Our sample is limited to galaxies more luminous than the SDSS r-band magnitude limit at the median redshift of the von der Linden et al. (2010) cluster sample, so our sample is on average more massive than theirs. However, the timescale for dynamical friction to affect cluster members is much longer than the Hubble time. This suggests that cluster galaxies undergo mass segregation via virial relaxation, analogous to the mass segregation exhibited by some Galactic globular clusters.

We measured the fractions of SFGs in our cluster sample as a function of redshift, and we found that these fractions are consistent with the measurements made by Haines et al. (2009) for the LoCuSS clusters. However, incomplete AGN subtraction can introduce significant contamination to the integrated star formation in galaxy clusters. For example, we found that eliminating only X-ray AGNs from the sample prior to calculation of f_{SF} results in a $\sim 1\sigma$ excess in AC 114 in Figure 11. The consequences are both more significant and more widespread for lower SFR thresholds. This can bias measurements of star formation

as a function of redshift, since the AGN contribution is expected to be more significant at higher redshift (Martini et al. 2009). With a long enough redshift baseline, evolution in f_{SF} with cosmic time can probe the timescale for the end of star formation in cluster galaxies. Present observations favor gas starvation over RPS, but these include important systematic uncertainties.

On balance, our measurements are most consistent with RPS as the primary mechanism to reduce star formation in cluster galaxies. The SFR–radius relation agrees better with the predictions of RPS than with gas starvation over the range of radii that we study. This supports the conclusions of Bai et al. (2009), who studied star formation in clusters over a similar range of radii and determined that RPS dominates the reduction of SFR among cluster galaxies. The observation that SFR does not correlate strongly with M_* among SFGs in clusters can be explained by the concentration of massive galaxies near the cluster center, where RPS operates most efficiently. Furthermore, Bai et al. (2009) also found that the luminous end of the TIR LF does not vary significantly between $z = 0$ clusters, and we similarly find that the redshift-appropriate field galaxy LF provides a good match to the observed TIR LF in each cluster. While this is also consistent with RPS as the primary mechanism to end star formation among cluster galaxies, the disagreement between the field galaxy LF and the stacked cluster sample suggests that there are small deviations between the individual clusters and the field galaxy LF that we overlook due to limited precision in the measured LFs. Such deviations would be more consistent with gas starvation than with RPS. Additionally, the long timescale we infer for the evolution of f_{SF} conflicts with the conclusion that RPS ends star formation among cluster members and is more consistent with gas starvation. This evidence agrees with the conclusions of Verdugo et al. (2008) and von der Linden et al. (2010), who found independent evidence in favor of gas starvation. A measurement of the rate of change in f_{SF} as a function of redshift can provide an additional line of evidence to help resolve this disagreement. Present results favor a long timescale, but these include significant systematic uncertainties. A measurement with a single sample of uniformly analyzed clusters will be the subject of our next paper.

We are grateful to Kim-Vy Tran and Dan Kelson for insightful comments on an earlier version of this paper and to John Mulchaey for helpful discussions. DWA thanks The Ohio State University for support via the Dean's Distinguished University Fellowship. PM is grateful for support from the NSF via award AST-0705170. This work is based in part on observations made with the *Spitzer Space Telescope*, which is operated by the Jet Propulsion Laboratory, California Institute of Technology under a contract with NASA. Support for this work was provided by NASA through an award issued by JPL/Caltech. This research has made use of the NASA/IPAC Extragalactic Database (NED) which is operated by the Jet

Propulsion Laboratory, California Institute of Technology, under contract with the National Aeronautics and Space Administration.

A. Asymmetric Distribution Function

In order to apply the method described in §5 to construct a luminosity function, we must smoothly distribute the weight of a galaxy across the specified luminosity bins. The method described in §5.1 to calculate L_{TIR} produces asymmetric uncertainties, $L_{TIR} = \mu^{+\sigma_u}_{-\sigma_l}$, so we need an asymmetric probability density function (PDF) to distribute weights correctly. This PDF must reduce to the Normal distribution in the case when the upper and lower luminosity uncertainties are equal (i.e. Gaussian errors). Here, we describe a piecewise smooth function that satisfies these requirements.

First, we define an effective dispersion $\sigma_e = \sqrt{\sigma_l \sigma_u}$, where σ_u and σ_l are the upper and lower uncertainties on L_{TIR}, respectively. We then define an alternative dispersion, $\sigma(L)$, which describes the instantaneous shape of the PDF at a luminosity L,

$$\sigma(L) = \begin{cases} \sigma_l & \text{IF } L < \mu - \sigma_l \\ \sigma_e + (\sigma_l - \sigma_e)\frac{|L-\mu|}{\sigma_l} & \text{IF } \mu - \sigma_l \leq L < \mu \\ \sigma_e & \text{IF } L = \mu \\ \sigma_e + (\sigma_u - \sigma_e)\frac{|L-\mu|}{\sigma_u} & \text{IF } \mu < L \leq \mu + \sigma_u \\ \sigma_u & \text{IF } \mu + \sigma_u < L \end{cases} \tag{A1}$$

where μ is the best estimate L_{TIR}; σ_u and σ_l are the upper and lower uncertainties on μ, respectively. $\sigma(L)$ smoothly connects the low-L and high-L tails of the desired distribution function. Given $\sigma(L)$, we can calculate the probability density for a galaxy with measured luminosity μ at L. This probability density is given by,

$$f(L, \mu, \sigma_u, \sigma_l) = \frac{1}{\sqrt{2\pi}\ \sigma(L)} e^{-(\mu-L)^2/2\sigma^2(L)} \tag{A2}$$

where $\sigma(L)$ is given by Eq. A1.

The PDF described by Eqs. A1 and A2 approaches Gaussian at the high- and low-L extremes, with dispersions σ_u and σ_l, respectively. It also smoothly connects these two limiting cases, integrates to unity, and has dispersion equal to the geometric mean of σ_l and σ_u at the nominal luminosity. It therefore gives a PDF for the luminosity of a given galaxy that satisfies our requirements and that is consistent with the available information about L_{TIR}.

REFERENCES

Abadi, M. G., Moore, B., & Bower, R. G. 1999, MNRAS, 308, 947

Abraham, R. G., et al. 1996, ApJ, 471, 694

Assef, R. J., et al. 2010, ApJ, 713, 970

Atlee, D. W., Martini, P., Assef, R. J., Kelson, D. D., & Mulchaey, J. S. 2011, ApJ, 729, 22

Bai, L., Rieke, G. H., Rieke, M. J., Christlein, D., & Zabludoff, A. I. 2009, ApJ, 693, 1840

Bai, L., Rieke, G. H., Rieke, M. J., Hinz, J. L., Kelly, D. M., & Blaylock, M. 2006, ApJ, 639, 827

Balogh, M. L., Baldry, I. K., Nichol, R., Miller, C., Bower, R., & Glazebrook, K. 2004, ApJ, 615, L101

Balogh, M. L., Morris, S. L., Yee, H. K. C., Carlberg, R. G., & Ellingson, E. 1997, ApJ, 488, L75+

Balogh, M. L., Navarro, J. F., & Morris, S. L. 2000, ApJ, 540, 113

Barkhouse, W. A., Yee, H. K. C., & López-Cruz, O. 2009, ApJ, 703, 2024

Bekki, K., Couch, W. J., & Shioya, Y. 2002, ApJ, 577, 651

Bell, E. F., & de Jong, R. S. 2001, ApJ, 550, 212

Berrier, J. C., Stewart, K. R., Bullock, J. S., Purcell, C. W., Barton, E. J., & Wechsler, R. H. 2009, ApJ, 690, 1292

Bertin, E., & Arnouts, S. 1996, A&AS, 117, 393

Bigiel, F., et al. 2011, ArXiv e-prints

Blanton, M. R., & Berlind, A. A. 2007, ApJ, 664, 791

Book, L. G., & Benson, A. J. 2010, ApJ, 716, 810

Braglia, F. G., Pierini, D., Biviano, A., & Böhringer, H. 2009, A&A, 500, 947

Butcher, H., & Oemler, Jr., A. 1978, ApJ, 219, 18

—. 1984, ApJ, 285, 426

Christlein, D., & Zabludoff, A. I. 2005, ApJ, 621, 201

Cowie, L. L., Songaila, A., Hu, E. M., & Cohen, J. G. 1996, AJ, 112, 839

Dale, D. A., & Helou, G. 2002, ApJ, 576, 159

De Lucia, G., Weinmann, S., Poggianti, B., Aragon-Salamanca, A., & Zaritsky, D. 2011, ArXiv e-prints

Dressler, A. 1980, ApJ, 236, 351

Dressler, A., & Shectman, S. A. 1988, AJ, 95, 985

Dressler, A., Smail, I., Poggianti, B. M., Butcher, H., Couch, W. J., Ellis, R. S., & Oemler, Jr., A. 1999, ApJS, 122, 51

Dressler, A., Thompson, I. B., & Shectman, S. A. 1985, ApJ, 288, 481

Dressler, A., et al. 1997, ApJ, 490, 577

Dunkley, J., et al. 2009, ApJS, 180, 306

Eggen, O. J., Lynden-Bell, D., & Sandage, A. R. 1962, ApJ, 136, 748

Ellis, R. 1987, in IAU Symposium, Vol. 124, Observational Cosmology, ed. A. Hewitt, G. Burbidge, & L. Z. Fang, 367–381

Fujita, Y. 2004, PASJ, 56, 29

Gill, S. P. D., Knebe, A., & Gibson, B. K. 2005, MNRAS, 356, 1327

Gisler, G. R. 1978, MNRAS, 183, 633

Grützbauch, R., Conselice, C. J., Varela, J., Bundy, K., Cooper, M. C., Skibba, R., & Willmer, C. N. A. 2011, MNRAS, 411, 929

Gunn, J. E., & Gott, III, J. R. 1972, ApJ, 176, 1

Haines, C. P., et al. 2009, ApJ, 704, 126

Hansen, S. M., Sheldon, E. S., Wechsler, R. H., & Koester, B. P. 2009, ApJ, 699, 1333

Hatch, N. A., Kurk, J. D., Pentericci, L., Venemans, B. P., Kuiper, E., Miley, G. K., & Röttgering, H. J. A. 2011, ArXiv e-prints

Jáchym, P., Palouš, J., Köppen, J., & Combes, F. 2007, A&A, 472, 5

Kauffmann, G., White, S. D. M., Heckman, T. M., Ménard, B., Brinchmann, J., Charlot, S., Tremonti, C., & Brinkmann, J. 2004, MNRAS, 353, 713

Kawata, D., & Mulchaey, J. S. 2008, ApJ, 672, L103

Kendell, M. G., & Stuart, A. J. 1977, Advanced Theory of Statistics (Halsted Press)

Kenney, J. D. P., van Gorkom, J. H., & Vollmer, B. 2004, AJ, 127, 3361

Kodama, T., & Bower, R. G. 2001, MNRAS, 321, 18

Kümmel, M. W., & Wagner, S. J. 2001, A&A, 370, 384

Lake, G., Katz, N., & Moore, B. 1998, ApJ, 495, 152

Larson, R. B., Tinsley, B. M., & Caldwell, C. N. 1980, ApJ, 237, 692

Le Floc'h, E., et al. 2005, ApJ, 632, 169

Martini, P., Kelson, D. D., Kim, E., Mulchaey, J. S., & Athey, A. A. 2006, ApJ, 644, 116

Martini, P., Mulchaey, J. S., & Kelson, D. D. 2007, ApJ, 664, 761

Martini, P., Sivakoff, G. R., & Mulchaey, J. S. 2009, ApJ, 701, 66

McCarthy, I. G., Frenk, C. S., Font, A. S., Lacey, C. G., Bower, R. G., Mitchell, N. L., Balogh, M. L., & Theuns, T. 2008, MNRAS, 383, 593

Merloni, A., Heinz, S., & di Matteo, T. 2003, MNRAS, 345, 1057

Merritt, D. 1983, ApJ, 264, 24

—. 1984, ApJ, 276, 26

Moore, B., Katz, N., Lake, G., Dressler, A., & Oemler, A. 1996, Nature, 379, 613

Moore, B., Lake, G., & Katz, N. 1998, ApJ, 495, 139

Moran, S. M., Ellis, R. S., Treu, T., Salim, S., Rich, R. M., Smith, G. P., & Kneib, J.-P. 2006, ApJ, 641, L97

Moran, S. M., Ellis, R. S., Treu, T., Smith, G. P., Rich, R. M., & Smail, I. 2007, ApJ, 671, 1503

Natarajan, P., Kneib, J., Smail, I., & Ellis, R. S. 1998, ApJ, 499, 600

Oemler, Jr., A. 1974, ApJ, 194, 1

Osterbrock, D. E. 1960, ApJ, 132, 325

Patel, S. G., Holden, B. P., Kelson, D. D., Illingworth, G. D., & Franx, M. 2009, ApJ, 705, L67

Pérez-González, P. G., et al. 2005, ApJ, 630, 82

Pimbblet, K. A. 2011, MNRAS, 411, 2637

Poggianti, B. M., Smail, I., Dressler, A., Couch, W. J., Barger, A. J., Butcher, H., Ellis, R. S., & Oemler, Jr., A. 1999, ApJ, 518, 576

Poggianti, B. M., et al. 2006, ApJ, 642, 188

—. 2008, ApJ, 684, 888

Postman, M., & Geller, M. J. 1984, ApJ, 281, 95

Postman, M., et al. 2005, ApJ, 623, 721

Quilis, V., Moore, B., & Bower, R. 2000, Science, 288, 1617

Rettura, A., et al. 2011, ArXiv e-prints

Roediger, E., & Brüggen, M. 2006, MNRAS, 369, 567

—. 2007, MNRAS, 380, 1399

Roediger, E., & Hensler, G. 2005, A&A, 433, 875

Saintonge, A., Tran, K., & Holden, B. P. 2008, ApJ, 685, L113

Simard, L., et al. 2009, A&A, 508, 1141

Sivanandam, S., Rieke, M. J., & Rieke, G. H. 2010, ApJ, 717, 147

Spitzer, Jr., L., & Baade, W. 1951, ApJ, 113, 413

Takeuchi, T. T., Buat, V., Iglesias-Páramo, J., Boselli, A., & Burgarella, D. 2005, A&A, 432, 423

Tran, K., et al. 2010, ApJ, 719, L126

Treu, T., Ellis, R. S., Kneib, J., Dressler, A., Smail, I., Czoske, O., Oemler, A., & Natarajan, P. 2003, ApJ, 591, 53

van Daalen, M. P., Schaye, J., Booth, C. M., & Dalla Vecchia, C. 2011, ArXiv e-prints

Verdugo, M., Ziegler, B. L., & Gerken, B. 2008, A&A, 486, 9

von der Linden, A., Best, P. N., Kauffmann, G., & White, S. D. M. 2007, MNRAS, 379, 867

von der Linden, A., Wild, V., Kauffmann, G., White, S. D. M., & Weinmann, S. 2010, MNRAS, 404, 1231

Wall, J., & Jenkins, C. 2003, Practical Statistics for Astronomers (Cambridge University Press), 66–67

Whipple, F. L. 1946, ApJ, 104, 1

White, S. D. M., & Frenk, C. S. 1991, ApJ, 379, 52

Yan, R., et al. 2009, MNRAS, 398, 735

Zabludoff, A. I., & Mulchaey, J. S. 1998, ApJ, 496, 39

Zhu, Y., Wu, H., Cao, C., & Li, H. 2008, ApJ, 686, 155

Table 1. Spectroscopic Completeness

	m_R (Vega)	R/R_{200}	$f_{Cl,spec}$	σ_f
a3128	14.33	0.11	0.669	0.016
	15.76	0.10	0.682	0.042
	16.32	0.07	1.020	0.065
	16.89	0.06	0.532	0.057
a3125	14.60	0.17	0.000	0.000
	15.92	0.22	0.000	0.000
	16.29	0.05	1.000	0.000
	16.77	0.16	0.000	0.000
a2104	17.28	0.05	0.719	0.015
	18.32	0.07	0.249	0.007
	18.88	0.11	0.222	0.008
	19.31	0.11	0.068	0.003
a1689	17.02	0.03	0.626	0.014
	18.46	0.08	0.409	0.014
	19.07	0.09	0.217	0.015
	19.65	0.12	0.411	0.033
ms1008	19.10	0.08	0.693	0.054
	19.79	0.04	0.293	0.013
	20.35	0.08	0.225	0.014
	20.91	0.11	0.084	0.010
ac114	19.00	0.10	0.744	0.069
	19.84	0.06	0.925	0.072
	20.37	0.13	0.399	0.050
	20.83	0.14	0.913	0.353

Note. — A sample of spectroscopic completeness measurements as described in §4.1. The complete table is available from the electronic edition of the journal. A brief sample is shown here for guidance regarding form and content.

Table 2. MIR Completeness

(1)	R/R_{200} (2)	$f_\nu(8\mu m)$ $[Jy]$ (3)	$C_{8\mu m}$ (4)	$f_\nu(24\mu m)$ $[Jy]$ (5)	$C_{24\mu m}$ (6)
A3128	0.06	2.65×10^{-4}	$0.00^{+0.15}_{-0.00}$	1.70×10^{-4}	$0.00^{+0.15}_{-0.00}$
	0.06	8.44×10^{-4}	$0.51^{+0.18}_{-0.17}$	5.41×10^{-4}	$0.00^{+0.15}_{-0.00}$
	0.06	2.69×10^{-3}	$0.55^{+0.14}_{-0.20}$	1.64×10^{-3}	$0.31^{+0.16}_{-0.17}$
	0.06	8.57×10^{-3}	$0.55^{+0.14}_{-0.20}$	5.44×10^{-3}	$1.00^{+0.00}_{-0.19}$
	0.06	2.66×10^{-2}	$0.55^{+0.14}_{-0.20}$	1.74×10^{-2}	$1.00^{+0.00}_{-0.19}$
	0.06	8.48×10^{-2}	$0.55^{+0.14}_{-0.20}$	5.51×10^{-2}	$1.00^{+0.00}_{-0.19}$
	0.06	2.73×10^{-1}	$0.55^{+0.14}_{-0.20}$	1.64×10^{-1}	$1.00^{+0.00}_{-0.19}$
	0.06	8.67×10^{-1}	$0.55^{+0.14}_{-0.20}$	5.49×10^{-1}	$1.00^{+0.00}_{-0.19}$
A3125	0.05	2.53×10^{-4}	$0.00^{+0.50}_{-0.00}$	1.58×10^{-4}	$0.00^{+0.50}_{-0.00}$
	0.05	7.95×10^{-4}	$1.00^{+0.00}_{-0.50}$	5.09×10^{-4}	$0.00^{+0.50}_{-0.00}$
	0.05	2.40×10^{-3}	$1.00^{+0.00}_{-0.50}$	1.57×10^{-3}	$0.00^{+0.50}_{-0.00}$
	0.05	7.89×10^{-3}	$1.00^{+0.00}_{-0.50}$	5.03×10^{-3}	$0.58^{+0.08}_{-0.08}$
	0.05	2.50×10^{-2}	$1.00^{+0.00}_{-0.50}$	1.60×10^{-2}	$1.00^{+0.00}_{-0.50}$
	0.05	7.84×10^{-2}	$1.00^{+0.00}_{-0.50}$	4.93×10^{-2}	$1.00^{+0.00}_{-0.50}$
	0.05	2.56×10^{-1}	$1.00^{+0.00}_{-0.50}$	1.57×10^{-1}	$1.00^{+0.00}_{-0.50}$
	0.05	8.01×10^{-1}	$1.00^{+0.00}_{-0.50}$	4.87×10^{-1}	$1.00^{+0.00}_{-0.50}$
A2104	0.06	3.43×10^{-5}	$0.00^{+0.06}_{-0.00}$	2.25×10^{-5}	$0.00^{+0.06}_{-0.00}$
	0.15	1.13×10^{-4}	$0.11^{+0.09}_{-0.06}$	6.91×10^{-5}	$0.03^{+0.07}_{-0.03}$
	0.24	3.47×10^{-4}	$0.51^{+0.17}_{-0.22}$	2.27×10^{-4}	$0.00^{+0.17}_{-0.00}$
	0.06	3.55×10^{-3}	$1.00^{+0.00}_{-0.03}$	2.21×10^{-3}	$0.68^{+0.09}_{-0.10}$
	0.15	1.10×10^{-2}	$0.93^{+0.04}_{-0.07}$	6.65×10^{-3}	$0.73^{+0.09}_{-0.09}$
	0.24	3.63×10^{-2}	$0.70^{+0.11}_{-0.23}$	2.16×10^{-2}	$0.80^{+0.14}_{-0.21}$
A1689	0.06	2.31×10^{-5}	$1.00^{+0.00}_{-0.09}$	1.42×10^{-5}	$0.00^{+0.06}_{-0.00}$
	0.06	7.49×10^{-5}	$1.00^{+0.00}_{-0.09}$	4.56×10^{-5}	$0.00^{+0.06}_{-0.00}$
	0.06	2.33×10^{-4}	$1.00^{+0.00}_{-0.09}$	1.43×10^{-4}	$0.04^{+0.08}_{-0.03}$
	0.06	7.17×10^{-4}	$1.00^{+0.00}_{-0.09}$	4.45×10^{-4}	$0.71^{+0.09}_{-0.13}$
	0.06	2.23×10^{-3}	$1.00^{+0.00}_{-0.09}$	1.45×10^{-3}	$0.81^{+0.09}_{-0.11}$
	0.06	7.10×10^{-3}	$1.00^{+0.00}_{-0.09}$	4.32×10^{-3}	$0.81^{+0.09}_{-0.11}$
	0.06	2.35×10^{-2}	$1.00^{+0.00}_{-0.09}$	1.43×10^{-2}	$0.81^{+0.09}_{-0.11}$
	0.06	7.38×10^{-2}	$1.00^{+0.00}_{-0.09}$	4.54×10^{-2}	$0.81^{+0.09}_{-0.11}$
MS1008	0.07	2.53×10^{-6}	$0.00^{+0.11}_{-0.00}$	0.00×10^{0}	$-1.00^{+1.00}_{-1.00}$
	0.07	7.55×10^{-6}	$0.00^{+0.11}_{-0.00}$	4.66×10^{-6}	$0.00^{+0.11}_{-0.00}$
	0.07	2.37×10^{-5}	$0.10^{+0.17}_{-0.05}$	1.43×10^{-5}	$0.00^{+0.11}_{-0.00}$
	0.07	7.69×10^{-5}	$1.00^{+0.00}_{-0.09}$	4.63×10^{-5}	$0.00^{+0.11}_{-0.00}$
	0.07	2.41×10^{-4}	$1.00^{+0.00}_{-0.09}$	1.52×10^{-4}	$0.00^{+0.11}_{-0.00}$
	0.07	7.67×10^{-4}	$1.00^{+0.00}_{-0.09}$	4.54×10^{-4}	$0.00^{+0.11}_{-0.00}$
	0.07	2.46×10^{-3}	$1.00^{+0.00}_{-0.09}$	1.43×10^{-3}	$0.00^{+0.11}_{-0.00}$
	0.07	7.48×10^{-3}	$1.00^{+0.00}_{-0.09}$	4.42×10^{-3}	$0.00^{+0.11}_{-0.00}$
	0.07	2.24×10^{-2}	$1.00^{+0.00}_{-0.09}$	1.48×10^{-2}	$0.00^{+0.11}_{-0.00}$
AC114	0.06	2.43×10^{-6}	$0.00^{+0.07}_{-0.00}$	0.00×10^{0}	$-1.00^{+1.00}_{-1.00}$
	0.06	7.10×10^{-6}	$0.00^{+0.07}_{-0.00}$	4.48×10^{-6}	$0.00^{+0.07}_{-0.00}$
	0.06	2.16×10^{-5}	$0.89^{+0.08}_{-0.11}$	1.35×10^{-5}	$0.00^{+0.07}_{-0.00}$
	0.06	7.16×10^{-5}	$1.00^{+0.00}_{-0.09}$	4.33×10^{-5}	$0.04^{+0.08}_{-0.03}$
	0.06	2.16×10^{-4}	$1.00^{+0.00}_{-0.09}$	1.37×10^{-4}	$0.56^{+0.11}_{-0.11}$
	0.06	7.05×10^{-4}	$1.00^{+0.00}_{-0.09}$	4.43×10^{-4}	$0.56^{+0.11}_{-0.11}$

Table 2—Continued

(1)	R/R_{200} (2)	$f_\nu(8\mu m)$ $[Jy]$ (3)	$C_{8\mu m}$ (4)	$f_\nu(24\mu m)$ $[Jy]$ (5)	$C_{24\mu m}$ (6)
	0.06	2.20×10^{-3}	$1.00^{+0.00}_{-0.09}$	1.40×10^{-3}	$0.56^{+0.11}_{-0.11}$
	0.06	6.79×10^{-3}	$1.00^{+0.00}_{-0.09}$	4.28×10^{-3}	$0.56^{+0.11}_{-0.11}$
	0.06	2.14×10^{-2}	$1.00^{+0.00}_{-0.09}$	1.36×10^{-2}	$0.56^{+0.11}_{-0.11}$

Note. — Column (1) gives the cluster name. Column (2) gives the median radius, scaled to the virial radius of the cluster, of galaxies that go into the bin. Columns (3) and (5) give the median observed frame fluxes in the $8\mu m$ and $24\mu m$ channels, respectively, of the model SEDs that make up each bin. Fluxes are calculated by integrating model SEDs with random combinations of the Assef et al. (2010) star forming templates across the published instrument response functions. If the SFR inferred from the rest frame luminosities in the model SEDs are outside the range $10^{-2} < SFR/(1\ M_\odot\ yr^{-1}) < 10^2$, the associated fluxes are not included in the sample. Because the Assef et al. (2010) templates are not constructed to have identical SFRs in the $8\mu m$ and $24\mu m$ channels, this sometimes means that an SED with a valid SFR in one channel will not appear in another. When a flux bin is occupied in one channel and not in another, the empty channel has $f_\nu = 0$ and $C_\lambda = -1$. This is the case for the first flux bin in AC114. Columns (4) and (6) give the MIR completeness (C_λ) as defined in §4.2. The complete table is available from the electronic edition of the journal. A sample is shown here for guidance regarding form and content.

Table 3. Cluster Member Summary

Name (1)	RA (2)	Dec (3)	z (4)	M_* $[10^{10} M_\odot]$ (5)	SFR $[M_\odot\ yr^{-1}]$ (6)	δ (7)
a3128-001	03:30:37.7	-52:32:57.7	0.063	$3.2 \pm 0.7 \pm 1.9$	< 0.33	0.89
a3125-001	03:27:20.2	-53:28:34.6	0.062	$3.3 \pm 0.7 \pm 2.0$	5.1 ± 0.7	3.04
a644-005	08:17:25.8	-07:33:42.5	0.071	$0.1 \pm 0.0 \pm 0.1$	—	1.07
a2104-001	15:40:07.6	-03:17:06.8	0.153	$3.1 \pm 1.0 \pm 1.9$	< 0.20	1.33
a1689-004	13:11:29.5	-01:20:27.7	0.183	$67.1 \pm 18.2 \pm 22.9$	< 1.22	1.47
a2163-001	16:15:25.8	-06:09:26.4	0.200	< 1.4	< 0.50	1.99
ms1008-001	10:10:34.1	-12:39:52.7	0.308	$5.3 \pm 1.7 \pm 1.6$	< 0.87	0.81
ac114-001	22:58:52.3	-34:46:47.9	0.303	< 0.1	< 0.39	1.20

Note. — The properties of cluster member galaxies, determined using the methods described by Atlee et al. (2011). (1) The name of this object, which is identical to the name given in Table 2 of Atlee et al. (2011). (2-3) Positions of each object in J2000 coordinates, as determined from the *R*-band images of identified cluster members. (4) Redshifts of each object, as determined by Martini et al. (2006,2007) where available, or from the literature otherwise. (5) Stellar masses derived using mass-to-light ratios appropriate for each galaxy's color and assuming a scaled Salpeter IMF with Bruzual & Charlot population synthesis model (Bell & de Jong 2001, Table 4). The first uncertainty quoted gives the statistical error, and the second gives the systematic error. Systematic errors are derived by applying the M/L coefficients appropriate for a Salpeter IMF and the PÉGASE population synthesis model. (6) Star-formation rates either from the $8\mu m$ luminosity, the $24\mu m$ luminosity or by taking the geometric mean of the two, depending on the measurements available. Uncertainties include only statistical errors, and upper limits are quoted at 3σ in the more sensitive of the $8\mu m$ and $24\mu m$ bands. (7) Substructure parameter of (Dressler & Schectman 1988), $\delta = (11/\sigma^2) \times \left[(\bar{v}_{local} - \bar{v})^2 + (\sigma_{local} - \sigma)^2\right]$, where the local average velocities ($\bar{v}$) and velocity dispersions (σ) are calculated over the 10 nearest neighbors of each galaxy. The complete table is available from the electronic edition of the journal. A brief sample is shown here for guidance regarding form and content.

Table 4. Partial Correlation Results

(1)	(2)	Partial r_s (3)	Prob. (4)
SFR	M_*	+0.091	5.15×10^{-01}
SFR	R/R_{200}	+0.342	2.11×10^{-05}
SFR	δ	−0.101	5.26×10^{-01}
SFR	Σ	+0.018	8.40×10^{-01}
M_*	R/R_{200}	−0.087	5.14×10^{-01}
M_*	δ	−0.024	7.93×10^{-01}
M_*	Σ	−0.012	8.90×10^{-01}
R/R_{200}	δ	+0.188	2.77×10^{-02}
R/R_{200}	Σ	−0.576	1.96×10^{-17}
δ	Σ	+0.068	5.41×10^{-01}

Note. — Partial correlation results for star forming galaxies derived from the Spearman correlation coefficients for the variables listed in columns (1) and (2). Column (3) gives the strength of the correlation between the two variables with the other parameters held fixed. Column (4) gives the probability that a correlation at least as strong as that observed might occur by chance among intrinsically uncorrelated data.